An absolute quantification atlas of small non-coding RNAs across diverse mammalian tissues and cell lines

Wen Xiao[1,†], Yuli Zheng[1,†], Hongdao Zhang[1,†,*], Beiying Xu[1,†], Ruiwen Zhang[1], Ligang Wu[1,*]

[1.] Key Laboratory of RNA Science and Engineering, Shanghai Institute of Biochemistry and Cell Biology, Center for Excellence in Molecular Cell Science, Chinese Academy of Sciences, University of Chinese Academy of Sciences, Shanghai, 200031, China.

† The first four authors contributed equally to this work.

* To whom correspondence should be addressed.

Ligang Wu, Email: lgwu@sibcb.ac.cn

Hongdao Zhang, Email: zhanghongdao6@sibcb.ac.cn

ABSTRACT

The low quantitative accuracy of conventional small noncoding RNA sequencing (sncRNA-seq) methods due to extensive ligation bias commonly limits functional investigation of microRNAs (miRNAs) and PIWI-interacting RNAs (piRNAs). Here, we developed qMap-seq, a single-tube sncRNA-seq protocol designed to minimize bias in the absolute quantification of miRNA and piRNA transcripts through the incorporation of quantitative exogenous RNA spike-ins. With qMap-seq, we profiled sncRNA expression across 20 murine tissues, 18 macaque tissues, and 24 widely used cell lines to establish a comprehensive quantitative reference atlas. Compared with existing small RNA databases, our data revealed substantial biases in miRNA abundance, strand selection, and tissue-specific expression at both individual and family levels. To further extend its utility, we employed machine learning to model and correct biases in conventional datasets, effectively recovering ground truth transcript abundances. All qMap-seq data and the accompanying bias-correction model are freely available via SmRNAQuant (http://wulg-lab.sibcb.ac.cn/SmRNAQuant/), a web-based repository for exploring sncRNA expression. Together, the qMap-seq, bias-correction model, and SmRNAQuant provide powerful resources to advance sncRNA research.

INTRODUCTION

Small non-coding RNAs (sncRNAs), including microRNAs (miRNAs), small interfering RNAs (siRNAs), and piwi-interacting RNAs (piRNAs), are key regulators in a variety of biological and pathological processes such as organ development, epigenetic modification, and tumorigenesis [1-8]. Numerous recent studies have greatly expanded our understanding of the diversity, complexity, and function of these sncRNAs [9-19]. Given their critical regulatory roles, a robust and comprehensive understanding of their biological functions requires accuracy in sncRNA profiling and quantification [20]. Despite the power and versatility of next-generation sequencing tools for studying sncRNA expression [21, 22], conventional sncRNA library construction typically relies on T4 RNA ligase for adapter ligation prior to reverse transcription and amplification, which are prone to introducing biases in quantification [23-26]. These biases primarily arise from the structure-dependent mechanism of T4-mediated ligation of adapters to sncRNAs, in addition to PCR amplification of cDNA library, both of which lead to over- or under-representation of specific sncRNAs that can ultimately skew conclusions about biological function [27-31].

Several methods have been developed to reduce or minimize these biases, including the use of terminal randomized adapter sequences and/or high polyethylene glycol (PEG) concentrations, as reported in methods such as 4N-seq, AQ-seq, IsoSeek, and NEXTflex [9, 15, 29-35]. Despite these advances, the large majority of sequencing approaches primarily target miRNAs with a 2'-hydroxyl group (2'-OH) at the 3' end, which neglects optimization of ligation efficiency for piRNAs and plant miRNAs, which instead harbor 3' 2'-O-methyl modifications (2'-Ome) that hinder ligation [15, 36-39]. Furthermore, many of these methods do not incorporate unique molecular identifiers (UMIs) to correct for PCR bias by eliminating duplicate sequences. Additionally, few of these sequencing approaches has been adopted to determine absolute quantification of sncRNA, which is essential for addressing crucial fundamental research questions related to sncRNA stoichiometry. For example, understanding the precise miRNA concentrations required for regulatory function can be vital to identifying differences between physiological and pathological processes

[40, 41]. Moreover, existing miRNA databases—such as miRbase [42], MirGeneDB [43], miRmine [44], and DIANA-miTED [45]—as well as tissue atlas of sncRNAs [46, 47], were constructed using such biased sncRNA sequencing data, and therefore lack the capacity for accurate absolute quantification. Consequently, a comprehensive, bias-minimized, and quantitatively accurate reference for sncRNAs has yet to be established.

To overcome these challenges, in the current study, we developed qMap-seq, a **q**uantitative **m**iRNA **a**nd **p**iRNA sequencing technique that minimizes bias in small RNA sequencing through innovations in adapter design and incorporation of exogenous RNA spike-ins. We applied qMap-seq to generate a comprehensive reference atlas of sncRNA expression by profiling 244 samples, including 20 tissues from mice, 18 tissues from crab-eating macaques, and 24 commonly used cell lines. To the best of our knowledge, this is the first and most systematic absolute quantification of sncRNAs across mammalian tissues and cell lines. To further expand its utility, we developed an XGBoost-based framework to correct biases in conventional datasets, enabling accurate reconstruction of ground truth transcript abundances. Additionally, we developed a web-based database to facilitate access to qMap-seq data, allowing researchers to retrieve and analyze small RNA expression profiles. Together, the qMap-seq method, correction model, and online resource constitute a robust platform for advancing both fundamental and clinical research in small noncoding RNAs.

RESULTS

Construction of qMap-seq with greatly reduced ligation bias for high accuracy sncRNA quantification

To construct qMap-seq, we modified the 4N-Xu method [35, 48] by first increasing the size of random nucleotides (NTs) in 5’ adapter from 4 to 7 NTs, while retaining a 3’ adapter of 4 random NTs that ensures a total of 11 random bases to reduce ligation bias and expand the number of unique molecular identifiers (UMIs) essential for removing duplicate reads. Based on AmpUMI model predictions [49] and previous

studies [34], we determined that UMIs with 11 random bases could effectively capture the most abundant molecules with low probability of UMI collision (1.4%, Supplementary Figure 1A). To limit the likelihood of generating excessive byproducts associated with long consecutive random sequences, we also introduced 3 fixed nucleotides into the 7 random nucleotides of the 5' adapter [50].

We then designed and synthesized 30 spike-ins, including 7 with 2'-O-methyl modifications at the 3' end, which enabled the evaluation of the quantitative accuracy of 2'-O-methyl-modified sncRNAs in addition to miRNAs. We prepared two spike-in pools, including an equimolar pool (EM) and a ratiometric pool (RM), to test the accuracy and uniformity of the library (Supplementary Figure 1B). In the ratiometric pool, the concentrations of 30 spike-ins spanned an approximate 2 x 10^5-fold concentration range, with 3 oligos per concentration.

Optimization of reaction conditions showed that, in addition to high PEG8000 concentration [32], the coefficient of variation (CV) of equimolar spike-ins gradually decreased with increasing concentration of adapters, suggesting that the higher concentration of adapters could further minimize potential library biases (Supplementary Figure 1C). However, higher adapter concentrations led to a significant increase in self-ligation byproducts, with up to 90% of raw data comprising such artifactual sequence that had to be discarded (Supplementary Figure 1D). To balance library uniformity and data quality, we determined that 0.55 μM was the optimal concentration of 3' and 5' adapters (Supplementary Figure 1E). Additionally, we found that Lambda exonuclease was more efficient than RecJ exonuclease in depleting excess 3' adapters [51] (Figure 1A and Supplementary Figure 1F).

We then evaluated the accuracy of qMap-seq by adding the EM or RM pools to total cellular RNAs and calculating the relative amounts of spike-ins based on the sequencing results. Compared to TruSeq and AQ-seq, qMap-seq demonstrated the lowest average CV (1.73 vs. 0.56 vs. 0.53 for TruSeq, AQ-seq, and qMap-seq, respectively), indicating a marked reduction in library ligation biases and resulting in more uniform representation of equimolar spike-ins (Figure 1B-C and Supplementary Figure 1G). Correlation analysis between the expected and observed abundance of

ratiometric spike-ins yielded Pearson's coefficients > 0.94, indicating that qMap-seq could accurately reflect small RNA expression levels across varying abundances (Figure 1D). Notably, in qMap-seq libraries, spike-ins with 3' end methylation showed similar ligation efficiency to non-methylated spike-ins (Supplementary Figure 1H), in sharp contrast to the TruSeq libraries, where spike-ins bearing terminal methylation were detected at over 10-fold lower efficiency compared to their non-methylated counterparts. This finding was further validated by the qMap library from mouse testis, which displayed a stronger 1U signal for piRNAs compared to the TruSeq library (Supplementary Figure 1I).

To assess the sensitivity of qMap-seq, we performed sequencing using serial dilutions of input RNA, ranging from microgram to nanogram (ng) and picogram (pg) levels. As a control, we compared miRNA expression profiles generated from 1 μg of input RNA with those from lower input amounts (Supplementary Figure 1J–K). The number of detected miRNA species remained relatively constant down to 10 ng of input RNA. Although reproducibility in miRNA detection declined moderately at 1 ng, Spearman correlation coefficients remained high (> 0.7). Below 1 ng, both the number of detected miRNA species and robustness dropped markedly. These results indicate that qMap-seq can faithfully profile sncRNA expression from as little as 1 ng of total RNA without substantial loss of performance.

Finally, we applied qMap-seq to quantify each small RNA by generating standard curves using the ratiometric spike-ins with known absolute molecule numbers. To validate its accuracy, we incorporated four additional external spike-ins and found that qMap-seq could predict the molar quantities of all spike-ins, except the lowest abundance one, with high precision (Pearson's coefficient = 0.93; predicted vs ground truth values; Figure 1E). Additionally, a comparison between miR-221-3p abundance in ten cell lines predicted by qMap-seq and miR-221-3p copy numbers obtained by qRT-PCR showed a high correlation (Pearson's coefficient = 0.93) between methods, further validating the quantitative accuracy of our method (Figure 1F). Notably, qMap-seq could accurately quantify sncRNAs with abundances >10 amol per 100 ng total RNAs.

Construction of a quantitative sncRNA expression atlas of mammalian tissues and cell lines

Assembling a set of tissues and cell lines commonly used in miRNA studies (Supplementary Dataset 1) resulted in a panel of 24 cell lines (n = 4), 20 tissues from BALB/C mice (n = 4), and 18 tissues from crab-eating monkeys (n = 4) (Figure 2A). Using qMap-seq, we then constructed 244 total libraries, among which 242 passed quality control screening (Figure 2B). Each library contained over 1 million genome-mapped reads (Supplementary Figure 2A), which were further annotated into various small ncRNA species (Figure 2B). Among these ncRNAs, miRNA was the most well-represented species in most cell lines and tissues, except in testis samples (Figure 2C). Correlation analysis of miRNAs between biological replicates showed expression correlations exceeding 0.9 (Supplementary Figure 2B-D), indicating high reproducibility.

Subsequent validation of quantitative accuracy for sncRNAs in each sample with an additional four spike-ins yielded a correlation coefficient of 0.97 between predicted and ground truth values (Supplementary Figure 2E-F), thereby confirming the accuracy of qMap-seq. This high accuracy enabled further estimation of the absolute abundance of each miRNA and piRNA in all cell lines and tissues in our panel, which we used to construct a dataset of “true” expression levels. We also noted that miRNA family quantifications had markedly low CV across biological replicates, further supporting the stability and reliability of absolute quantification by qMap-seq (Supplementary Figure 2G). Overall, these results indicated that qMap-seq generated robust, quantitative miRNA and piRNA expression datasets across a wide range of tissues and cell lines.

Comparative analysis of miRNA species and absolute expression across cell lines and tissues

We then applied these quantitative sncRNA datasets to analyze the number of miRNA species expressed in each cell line and tissue, mitigating the influence of

variations in sequencing depth by randomly selecting 1.5 million mapped molecules from each sample for analysis. In most cell lines, approximately 600 miRNA species were detected (Supplementary Dataset 2, Figure 3A), which was comparable to the 532 average miRNA species reported in the miRmine database [44]. Notably, U2OS cells had the highest number of miRNAs (715 species), while the fewest were detected in MDA-MB-231 cells (266 species). In tissue samples, typically more than 500 miRNA species were expressed, with the exception of erythrocytes and blood, which had only 328 species (Figure 3B). Of note, some samples with lower miRNA species numbers, e.g., erythrocytes and blood, also had a small subset of predominant or overrepresented miRNAs, such as miR-451. Intriguingly, we also observed that most samples from monkeys had fewer miRNA species compared to the corresponding tissues from mice, likely due to the less comprehensive miRNA annotation in monkeys.

We then compared absolute miRNA concentrations quantified by qMap-seq (Figure 3C-E). Similar to the distribution of miRNA species across samples, total miRNA contents were comparable among most cells, with absolute quantities averaging ~2200 amol per 100 ng of total RNAs (Supplementary Dataset 2, Figure 3C), or approximately 15 pg (~0.015% of total RNAs), which was consistent with previous reports [52]. Across cell lines, SH-SY5Y cells had the highest miRNA expression level, ~4000 amol per 100 ng total RNA. Across tissues, for example in monkeys, we found that brain samples had the lowest miRNA levels while heart and muscle samples had the highest. By contrast in mice, pancreas and testis tissues had the lowest miRNA levels, whereas skin samples had the highest miRNA contents (Supplementary Dataset 2, Figure 3D). As a result of this variability, Spearman analysis of miRNA concentrations between monkeys and mice tissues showed low correlation (R = 0.46; Figure 3D), potentially reflecting strong differences in miRNA expression among species. Additionally, due to the overrepresentation of miR-451 in blood and erythrocyte samples, absolute miRNA quantities were much higher in these samples compared to solid tissues.

Notably, although pancreas samples had a higher relative proportion of miRNAs

than testis in mice (Figure 2C), their absolute quantities were not significantly different (Figure 3D). These findings highlighted the importance of absolute quantification for comparing miRNA expression levels across different tissues or cell lines.

Improved miRNA expression accuracy with qMap-seq

Previous studies have shown that miRNA dosage influences the strength of downstream gene regulation, with highly expressed miRNAs commonly selected as key targets for further investigation [40, 41]. In our study, we focused on these highly expressed miRNAs across various cell lines and tissues, identifying notable discrepancies between qMap-seq datasets and the DIANA-miTED database, which shares the greatest overlap in cell lines with our study, as well as MirGeneDB, a well-established source for miRNA expression data in tissues. Absolute quantification with qMap-seq suggested that the expression levels of numerous miRNA species, including pre-miR-19, pre-miR-29, pre-miR-23a, pre-miR-24, pre-miR-126a, pre-miR-143, pre-miR-26a, and pre-miR-30c were likely underestimated in DIANA-miTED and MirGeneDB, while pre-let-7a, pre-let-7b, pre-let-7c, pre-miR-10a, pre-miR-22, and pre-miR-191 were overestimated in samples from the same tissues or cell lines (Supplementary Dataset 3).

To test whether these discrepancies arose through differences among library construction methods, we analyzed heterodimer structures for both over- and underestimated miRNAs, as the influence of heterodimer structures formed between RNA and adapters has been widely reported to influence T4 RNA ligase (Rnl) activity, wherein 5’ adapter ligation by Rnl1 favoring RNAs with an unpaired 5’ end [29, 30, 53-55]. This analysis of heterodimer structures in over- and underestimated miRNAs with 5’ RNA adapters revealed that over 85% of the overestimated miRNAs had unpaired 5’ ends, while around 70% of underestimated miRNAs had paired 5' ends (Supplementary Figure 3A-B), which was consistent Rnl1 bias for unpaired 5’ ends. By contrast, for qMap-seq data, generated with random adapters, over 90% of these underestimated miRNAs formed secondary structures more favorable for Rnl1 ligation (Supplementary Figure 3C). These findings suggested that qMap-seq consequently

improved the accuracy of miRNA expression quantitation, compared to that in DIANA-miTED or MirGeneDB.

Analysis of miRNA strand preference by qMap-seq

In addition to the above problem of over- or underrepresentation, ligation bias has also been identified as a potential source of mis-annotation in miRNA strand preference for certain miRNAs, such as pre-miR-423, pre-miR-17, pre-miR-106b, and pre-miR-151a. As bias-reducing methods have been shown to help mitigate this issue [29, 32], we next examined strand preference in qMap-seq data. This analysis showed that miRNA strand preferences were consistent with previously validated results for pre-miR-324 [56], pre-miR-423 [32], pre-miR-223 [57], and pre-miR-133a [58] (Figure 4A-B). Moreover, strand preferences measured by qMap-seq also correlated closely with those obtained by AQ-seq in the HCT116 and HEK293T cell lines (Pearson's coefficient = 0.94 and 0.91, respectively), whereas moderate differences were noted when compared to TruSeq (Pearson's coefficient = 0.79 for HCT116 cell line and 0.82 for HEK293T cell line; Figure 4C). Subsequent application of a strand selection model to all miRNA, as previously described [59], and compared with the strand ratio data obtained by qMap-seq and TruSeq showed that qMap-seq data shared a stronger correlation with model predictions (Pearson's coefficient = 0.67) than TruSeq (Pearson's coefficient = 0.59; Figure 4D), further emphasizing higher accuracy of qMap-seq in strand ratio measurements.

Examination of strand preference for all detected miRNAs across cell lines and tissues in our qMap-seq data (Supplementary dataset 4) indicated that >50% of miRNAs preferentially expressed the 5p strand, whereas >30% preferentially expressed the 3p strand, regardless of species (Figure 4E). Additionally, although most miRNAs exhibited consistent strand preferences, a small subset switched the preferred strand depending on the cell type or tissue (Figure 4A). For example, pre-miR-142a produced more 3p than 5p miRNAs in mouse blood, but more 5p than 3p miRNAs in other tissues. Likewise, pre-miR-324 and pre-miR-339 in monkeys, as well as pre-miR-126a and pre-miR-144 in mice, also showed variable strand

preferences. Notably, qMap-seq identified several miRNAs with opposite strand selection compared to TruSeq or miRBase annotations, including pre-miR-500a, pre-miR-582, pre-miR-671, and pre-miR-362 (Figure 4F), as well as 15 previously reported miRNAs, such as pre-miR-193a, pre-miR-374a, and pre-miR-454 [29]. Taken together, these results indicated that qMap-seq could provide more reliable and accurate miRNA strand preference data than other current methods.

Re-evaluation of the expression and tissue specificity of miRNA families

As miRNA families, which share a common seed sequence and exhibit high sequence similarity, often exert cumulative effects on gene expression [60-64]. However, the extent to which previous biased sequencing approaches affect the accurate measurement of miRNA family expression has not yet been evaluated. We therefore assessed miRNA family-level expression patterns across various cell lines and tissues for comparison with other current miRNA databases.

We observed that miRNA families such as let-7, miR-10, and miR-21 were broadly expressed across human cell lines in qMap-seq data (Figure 5A), which agreed well with previous reports [1, 44, 65, 66]. However, comparison with DIANA-miTED revealed significant discrepancies in certain miRNA family expression patterns compared with qMap-seq data. For example, miR-15, miR-17, miR-19, and miR-29 family expression levels were generally underestimated in DIANA-miTED, while the let-7, miR-10, miR-191, and miR-92 families were overrepresented compared to qMap-seq data (Figure 5B). Further, even more pronounced discrepancies emerged through comparisons of tissue level data between qMap-seq and MirGeneDB (Supplementary Figure 4A-B), which indicated that the miR-126, miR-143, miR-19, miR-23, miR-24, miR-26, and miR-29 families were generally underestimated, whereas let-7, miR-1, miR-103, miR-199, miR-10, miR-181, miR-191 and miR-22 families were overrepresented in MirGeneDB (Supplementary Figure 4C-D). Closer scrutiny of these datasets suggested that these discrepancies likely arose through inaccurate quantification of specific miRNAs, such as miR-19a and miR-19b in the miR-19 family, as well as miR-29a, miR-29b, and miR-29c in the miR-29 family, which

led to underestimation of these miRNA families by conventional small RNA sequencing analytical methods (Supplementary Dataset 3). Consistent with this, previous studies have also shown that miR-29b ranked only 29th in the fixed adapter library derived from DLD-1 cells, whereas it was the most abundant miRNA in the random adapter library [29]. This discrepancy illustrates how miR-29b might be overlooked in colorectal cancer studies. These cumulative results suggested that qMap-seq data could provide a more accurate reference for miRNA family expression, which is essential for elucidating their biological functions and roles in disease processes.

We then focused on identifying ubiquitously expressed or tissue-specific miRNA families, which revealed that the let-7, miR-10, miR-23, miR-24, miR-26, miR-27, miR-29, and miR-30 families were highly expressed across all solid tissues, and showed remarkably similar expression levels between mice and monkeys (Figure 5C). These results were in line with the well-documented roles of these miRNA families in various developmental, cellular, and physiological processes essential for most tissues [1]. In contrast with the above broadly expressed miRNAs, we next searched for tissue-specific miRNA families, which are particularly intriguing due to their potential for specialized functions within specific tissues [44, 67]. To assess tissue specificity, we calculated the tissue specificity index (TSI) for miRNA families using a well-established method [68], wherein higher TSI values indicated greater tissue specificity. This analysis uncovered 27 and 30 total tissue-specific miRNA families in qMap-seq data from monkey and mouse tissues, respectively (TSI ≥ 0.85, Table 1). Among these tissue-specific miRNA families, more than 75% were consistent with those identified by MirGeneDB (Figure 5D, Table 2-3), which may be attributable to the high accuracy of relative expression analysis available through all current small RNA sequencing methods [35].

However, we also found some noteworthy differences with qMap-seq results. First, the tissue-specific miRNA families identified using qMap-seq data were largely subsets of those identified using MirGeneDB (13 out of 17). For example, 7 of 11 brain-specific miRNA families identified by MirGeneDB in monkeys were also

detected using qMap-seq. Further analysis revealed that the miRNA families missed by qMap-seq were predominantly expressed at low levels (Figure 5E), and were likely filtered out due to the expression cut-off we applied during the analysis process. Alternatively, qMap-seq analysis identified five tissue-specific miRNA families that were overlooked by MirGeneDB, such as the kidney-specific miR-204 and miR-8 families and spleen-specific miR-146 and miR-335 families in monkey (Table 2), as well as the ovary-specific miR-135 in mouse (Table 3). The expression levels of these miRNA families may have been underestimated by conventional sequencing data compared to qMap-seq (Figure 5F), potentially leading to their omission from MirGeneDB. Taken together, the capacity for precise miRNA quantification by qMap-seq facilitates more reliable identification of tissue-specific miRNA families.

Tissue-specific miRNA families are conserved between mice and monkeys

Since tissue-specific miRNAs have been previously shown to exhibit high conservation between mice and humans [68, 69], we next applied qMap-seq to explore the conservation of tissue-specific miRNA families between mice and monkeys. Our results showed that TSI values were quite similar between species for these miRNA families (Pearson's coefficient = 0.79, Supplementary Figure 5A), which was consistent with their comparable expression profiles. This analysis also showed a high degree of overlap in the tissue-specific expression of miRNA families between the two species (Supplementary Figure 5B, Table 1). For example, we identified several well-documented tissue-specific miRNA families, such as the miR-122 family in liver; miR-9, miR-128, miR-137, and miR-124 families in brain; miR-133 and miR-1 family in muscle; miR-499 family in heart; miR-144 and miR-451 families in blood; miR-205 family in skin; and miR-216 family in the pancreas [46, 68, 70-73]. Additionally, we identified some previously unreported tissue-specific miRNA families in mice and monkeys, including the miR-203 family in the skin, miR-459 and miR-217 families in the pancreas, as well as miR-19 and miR-142 families in blood. These findings suggested that tissue-specific miRNA families are conserved across mouse and monkey tissues.

Machine learning-based correction of sequencing bias in sncRNA expression profiles

To enhance the utility of existing sncRNA sequencing datasets affected by library preparation bias, we developed a computational framework that corrects biases in conventional expression profiles, generating quantitatively accurate datasets. We analyzed matched samples processed using two protocols: the widely adopted NEBNext small RNA library preparation and our optimized qMap-seq method. Using these paired datasets, we trained XGBoost regression models to learn and correct library-specific artifacts present in conventional sequencing data (Figure 6A). The correction model exhibited strong performance in reconstructing accurate expression profiles from biased datasets. For NEBNext-prepared libraries, the predicted expression levels showed high concordance with those obtained from qMap-seq, with Pearson correlation coefficients of r = 0.89 in the test set and r = 0.85 in the validation set (Figure 6B). Importantly, the model also improved the ranking accuracy of transcript abundances: the correlation with qMap-seq data increased from r = 0.56 (uncorrected) to r = 0.84 (corrected) in the test set (Figure 6C). Internal validation further confirmed the robustness of the model, yielding similarly high correlations (Pearson's r = 0.86; Figure 6D). In summary, this regression-based correction framework enables accurate reinterpretation of existing sncRNA-seq datasets by mitigating protocol-induced biases.

SmRNAQuant: an integrated qMap-seq database

To facilitate access to our qMap-seq data from various cell lines and tissues, we developed SmRNAQuant (Figure 7), an interactive analytical and visualization platform incorporating Django (v4.2.1), Bootstrap (v3.3.7), jQuery (v3.2.1), Python 3.8, and Echarts. This platform enables detailed quantification of small RNAs across different cell lines and tissues, facilitating deeper insights into expression patterns and biological roles. Users can download the complete dataset or generate customized subsets by selecting specific tissues or cell lines of interest. SmRNAQuant also

features a “miRNA view” function, which allows users to query individual miRNAs and visualize their expression profiles through bar charts across various tissues and cell types, providing a comprehensive overview of miRNA expression. Additionally, the platform integrates our regression-based correction algorithm, enabling users to calibrate NEBNext-derived datasets and obtain expression values comparable to those generated by qMap-seq. Collectively, SmRNAQuant improves the accessibility and usability of small RNA sequencing data for a broad range of research applications.

DISCUSSION

It's well known that conventional ligation-based methods introduce various biases, leading to the development of several bias-minimized sncRNA sequencing methods [9, 15, 29-35]. However, none of these methods achieves the absolute quantification of sncRNAs, a capability that is essential for generating reliable reference datasets and for advancing our understanding of the regulatory roles of sncRNAs [46, 74]. In this study, we introduce qMap-seq, a bias-minimized and quantitatively calibrated method for absolute sncRNA profiling. We also introduce SmRNAQuant, a web-based database designed to host absolute quantification datasets of sncRNAs. To further enhance the usability of qMap-seq and SmRNAQuant, we developed a machine learning-based correction model to adjust for biases inherent in conventional sncRNA sequencing data. Together, our work provides the first large-scale and systematic atlas of absolute quantification of sncRNAs across a diverse range of mammalian tissues and widely used cell lines.

Compared with external databases, our datasets provide more accurate small RNA information. First, it offers a more precise ranking of miRNAs in tissues and cell lines, which is crucial for researchers to select research targets. For example, our results indicate that, compared to existing databases, the expression levels of the miR-29 and miR-19 families are significantly higher, whereas those of the miR-10 and let-7 families are significantly lower. These differences are mainly attributed to the structural preferences of the T4 ligation enzyme. Second, our datasets provide more

reliable information on miRNA strand preference, which is consistent with both experimental and model-based findings reported in the literature. Moreover, in comparison to TruSeq sequencing data and miRBase, we identified strand annotation deviations in certain miRNAs, such as pre-miR-500a and pre-miR-362, which could greatly affect the prediction of their target genes. Third, our datasets provide a higher signal-to-noise ratio for tissue-specific miRNAs, making it a more reliable dataset for studying miRNA conservation across species. In addition, we developed an XGBoost-based correction framework that converts conventional small RNA-seq data into quantitatively accurate expression profiles. By eliminating the need for re-sequencing, it substantially expands the value of existing data and facilitates more reliable downstream analyses. Leveraging the unbiased quantification provided by qMap-seq, SmRNAQuant integrates this correction model to serve as a more reliable and precise reference resource for small RNA research.

Despite its strengths, this study has several limitations. First, the effectiveness of qMap-seq for constructing sncRNA libraries depends on a minimum input of 1 ng of total RNA. Below this threshold, data quality declines markedly, primarily due to incomplete removal of excess 3' adapters, which leads to the accumulation of adapter–adapter PCR artifacts [48]. Future optimization efforts may focus on enhancing 3' adapter removal efficiency or exploring alternative strategies, such as using a cocktail of RNA ligases to reduce ligation bias and potentially eliminate the need for terminal degenerate sequences. Second, qMap-seq is specifically designed for quantifying sncRNAs that share compatible chemical termini (5' monophosphate and 3'-OH or 3'-O-methyl ends), such as miRNAs, siRNAs, and piRNAs. However, other classes of sncRNAs, including small nucleolar RNAs (snoRNAs), small nuclear RNAs (snRNAs), tRNA-derived small RNAs (tsRNAs), and rRNA-derived small RNAs (rsRNAs), often contain noncanonical 5' or 3' ends or internal modifications that interfere with ligation and reverse transcription in the current qMap-seq protocol. Several specialized methods have been developed to address these challenges [75-78], and integrating such techniques with qMap-seq may broaden its scope. Finally, the limited diversity of samples included in our current database may restrict

the generalizability of our findings and reduce the applicability of the data across broader biological contexts. To overcome this limitation, future studies should apply qMap-seq to a wider range of tissues, developmental stages, and disease states. In parallel, our machine learning–based correction framework offers a complementary solution by enabling integration and bias correction of existing sncRNA-seq datasets. Together, these efforts will expand sample representation and enhance the robustness and translational potential of the resulting small RNA expression database.

MATERIAL AND METHODS

Cell culture and RNA extraction

All cell lines were revived and cultured in a 6 cm dish at 37°C with 5% CO_2. Once the cells reached 90% confluence, they were collected with 1 mL of Trizol reagent (Invitrogen). Next, 200 µL of trichloromethane was added and mixed thoroughly. The solution was then centrifuged at 12,000 g for 15 minutes at 4°C. The upper aqueous phase (~450 µL) was transferred into a new 1.5 mL EP tube, followed by the addition of 900 µL of ethanol. The solution was mixed by inversion, left at -30°C for 30 minutes, and then centrifuged again at 12,000 g for 15 minutes at 4°C. After removing the supernatant, the pellet was washed twice with 80% ethanol, air-dried for 2-3 minutes at room temperature, and dissolved in DEPC-treated water. RNA concentration was measured using a Nanodrop spectrophotometer, and RNA quality was assessed using the Agilent Bioanalyzer 2200. Each RNA sample was diluted to a final concentration of 100 ng/µL and stored at -80°C until use.

Tissue collection and RNA extraction

BALB/c mice were purchased from Shanghai Lingchang Biotechnology Co., Ltd, and animal protocol was approved by the Center for Excellence in Molecular Cell Science, Chinese Academy of Sciences (SIBCBS2182005007). Crab-eating monkey tissues were generously provided by the Jinyi Chen' lab at Shanghai Institute of Materia Medica, Chinese Academy of Sciences.

Fresh blood samples were collected into EDTA anticoagulant tubes and diluted with PBS at a 1:1 ratio. 3mL of separation solution (Solarbio) and 3 mL of the diluted blood were added to a 15 mL centrifuge tube and centrifuged at 800 g for 30 minutes at room temperature, resulting in distinct layers containing plasma, white blood cells, separation solution, and red blood cells. The red blood cell layer was carefully transferred into a new 1.5 mL EP tube, mixed with 1 mL of Trizol, and stored at -20°C until RNA extraction. The white blood cell layer was transferred into a new 15 mL centrifuge tube, washed with 10 mL of PBS, and centrifuged at 250 g for 10 minutes at room temperature. After centrifugation, the supernatant was removed, and the

precipitate was resuspended with red blood cell lysis buffer, then centrifuged at 250 g for another 10 minutes. The supernatant was discarded, and the precipitate was resuspended with 1 mL Trizol. After thorough mixing, the sample was stored at -20°C until RNA extraction.

Mouse and monkey lung, breast, stomach, colon, rectum, kidney, brain, skin, liver, ovary, testis, fat, pancreas, heart, thymus, muscle, and spleen tissues were collected, cut into small pieces, and submerged in an appropriate amount of RNAlater (Thermo). After being stored overnight at 4°C, the samples were transferred to -20°C. For RNA extraction, 50-100 mg of tissue was ground using a cryogenic grinder or a mortar (see Supplementary Table 1 for the specific grinding method for each tissue), and RNA was purified as described above.

Small RNA spike-in design

We randomly generated 1,000 sequences with lengths ranging from 20 to 30 nt and predicted their secondary structures using RNAfold. Sequences were selected based on the following criteria: GC content between 40% and 60%, a predicted secondary structure with a ΔG greater than -3, and no alignment with common model organism genomes. Finally, 23 sequences were chosen as spike-in candidates. To evaluate the ligation efficiency of RNAs with 2'-Ome at the 3' ends, seven of these candidates were randomly selected. The 2'-OH at their 3' end was replaced by 2'-Ome, and one of their bases was altered to distinguish them from their 2'-OH counterparts. All spike-ins were synthesized by Suzhou Olipharma Co., Ltd.

Small RNA library preparation

One hundred nanograms of total RNA with 0.05 µL of 20 nM EM or RM spike-in control oligos was ligated to a 0.55 µM 3' randomized adapter using 25 U/µL T4 RNA ligase 2 truncated KQ (NEB) in 0.83X T4 RNA ligase reaction buffer (NEB), supplemented with 20% PEG 8000 (NEB) at 25°C overnight. The ligated RNA was then annealed with 1.28 µM RTP. To remove excess 3' adapters, 3.33 U/µL 5' deadenylase (NEB) and 0.2 U/µL lambda exonuclease (NEB) were added, followed

by incubation at 30°C for 1 hour and 37°C for 2 hours, respectively. Subsequently, the product was ligated to a 0.55 μM 5' randomized adapter using 0.4 U/μL of T4 RNA ligase 1 (NEB) in 0.74X T4 RNA ligase reaction buffer, supplemented with 0.7 mM ATP and 17.3% PEG 8000 (NEB) at 25°C for 1 hour. Reverse transcription was carried out using 5 U/μL of ProtoScriptII reverse transcriptase (NEB) in 1X ProtoScriptII RT reaction buffer (NEB), containing 0.5 mM dNTPs (Promega) and 10 mM DTT (NEB), at 50°C for 1 hour. The resulting cDNA was then amplified using 0.02 U/μL of KOD-Plus-Neo (TOYOBO) in 1X PCR Buffer, along with 0.5 μM of both forward and reverse primers, 1.5 mM $MgSO_4$ (TOYOBO), and 0.2 mM dNTPs (TOYOBO). After PCR amplification, the cDNA was gel-purified on a 6% polyacrylamide gel to remove adapter dimers and sequenced using the Illumina NovaSeq6000 sequencing system. The sequences of adapters, along with the sequences and specific mixing ratios of EM or RM spike-ins, are provided in Supplementary Table 2. Mouse tissue miRNA libraries (excluding blood, erythrocytes, and leukocytes) were also prepared using the NEBNext® Multiplex Small RNA Library Prep Set for Illumina®, with 100 ng of total RNA as input.

Quantitative real-time PCR

The reverse transcriptase reactions consisted of 100 ng of purified total RNA, 50 nM stem-loop RT primer, 1X reverse transcriptase M-MLV buffer (TAKARA), 0.25 mM of each dNTP (Promega), 10 U/μL of reverse transcriptase M-MLV RNase H- (TAKARA), and 1.07 U/μL of RNase inhibitor (Thermo). The total volume of the reactions was 7.5 μl, and they were incubated in a Bio-Rad T100 Thermal Cycler under the following conditions: 30 minutes at 25°C, 1 hour at 42°C, and 15 minutes at 75°C, before being held at 4°C. RT products were diluted five times with deionized water. Each real-time PCR assay for the microRNA (10 μL volume) contains 2 μL of diluted RT product, 5 μL of 2X Taq Pro Universal SYBR qPCR Master Mix (Vazyme), and 1.5 μM of both forward and reverse primers. The reactions were carried out in an Applied Biosystems® QuantStudio™ 6 Flex Real-Time PCR System in 384-well plates, with the following cycling conditions: an initial denaturation at 95°C for 30

seconds, followed by 40 cycles of denaturation at 95°C for 10 seconds and annealing/extension at 60°C for 30 seconds. The sequences of RT and PCR primers are listed in Supplementary Table 3.

Analysis of small RNA sequencing

Raw data (read1) were pre-processed using the FASTX Toolkit (v0.0.14). The first 70 bp of each read were retained, and low-quality sequences were filtered out (-q 20, -p 90). After quality filtering, adapter sequences were trimmed, requiring a minimum 10-nucleotide match at the 3' end. Reads without detected adapter or shorter than 32 bp were discarded. Only reads with "CGA" at positions 4-6 were retained, corresponding to the 5' random adapter. UMI extraction was performed with UMI_tools (v0.5.1) using the following parameters: extract --extract-method regex --bc-pattern="^(?P<umi_1>.[3])(?P<cell_1>.[3])(?P<umi_2>.[4])([A,T,C,G][5,100])(?P<umi_3>.[4])$". Processed reads were aligned to the target genome using Bowtie (v1.2.1.1) with parameters --best -v 0. Duplicate reads were removed with UMI_tools using the following parameters: dedup --edit-distance-threshold 1 --soft-clip-threshold 0 --method adjacency. Unaligned reads were mapped to the spike-in reference sequences using Bowtie with parameters --best -v 1 --norc and de-duplicated in the same manner. The remaining unmapped reads were aligned to the isomiR reference library with the same parameters and de-duplicated. Molecules aligned to the genome were merged with isomiR molecules for downstream analysis. Molecules were annotated based on the following priority: mature miRNA > isomiR > tRNA > rRNA > snoRNA > snRNA > scRNA > scaRNA > YRNA > lncRNA > mRNA > piRNA > novel miRNA. Mature miRNA, isomiR, piRNA, and novel miRNA were annotated based on exact sequence and length matches, while other small RNA categories were aligned to known sequences using Bowtie with parameters -k=100 -v=0 -norc. Reads that aligned to the genome but lacked known annotations were classified as "others". The expression of molecules in each library was normalized using the standard curve generated from the external spike-ins.

Prediction of novel miRNAs

To identify potential novel miRNAs in our library, we applied miRDeep2 (v0.1.2) to reads that did not align to known annotations. Novel miRNAs predicted by miRDeep2 were further filtered based on the following criteria: (1) no match to any known sequences in the Rfam database; (2) a total of at least 10 reads supporting the miRNA in the library; and (3) the mature miRNA sequence must have a corresponding star sequence. Only miRNAs that satisfied all three conditions were deemed reliable, and their precursor miRNA, mature miRNA, and star sequences were extracted. Additionally, if miRge3.0 predicted pre-miRNA sequences with expression from both strands, and the 3p or 5p strand had more than 10 reads and was not identified by miRDeep2, those sequences were incorporated into the miRDeep2 prediction results. Together, these sequences constituted the reference set for novel miRNAs.

Expression of miRNA families

To assess the expression patterns of miRNA families, we extracted all miRNA family annotations from the latest version of MirGeneDB (v2.1). For each miRNA precursor, all mature forms have been considered as family members. To reduce potential bias from multiple precursors, duplicated mature miRNAs (e.g., those derived from different precursors within the same family) were counted only once.

Prediction of miRNA arm ratio

We analyzed the miRNA arm ratio as previously described [59] with the following model:

$$In\left(\frac{5p}{3p}\right) = k\Delta\Delta G_{5p-3p} + \left(N_{5p} - N_{3p}\right)$$

Where k and $N_{5p(3p)}$ represent the constant for the relative thermodynamic stability and the constant corresponding to the 5′ end identity, respectively.

Tissue specificity index

To compute the tissue specificity index, we used the formula described previously described [68]. The same formula was applied to cells to provide a cell specificity index. Specifically, the TSI for a miRNA j is calculated as

$$TSI_j = \frac{\sum_{i=1}^{N} \left(1 - x_{j,i}\right)}{N - 1},$$

Where *N* is the total number of tissues measured and $x_{j,i}$ is the expression score of tissue *i* normalized by the maximal expression of any tissue for miRNA *j*.

Model development and validation

The correction model was developed using the XGBoost, a robust machine learning method known for its robustness and high predictive accuracy. Model training was conducted on the designated training dataset, with hyperparameter optimization performed using the Hyperopt package in Python. The final model architecture incorporated the following optimized parameters: a learning rate (eta) of 0.4, num_boost_round of 10, max_depth of 8, min_child_weight of 14, subsample of 0.75, colsample_bynode of 0.5, colsample_bytree of 1.0, and reg_lambda of 4.0. Model performance was evaluated on both a test set and an independent external validation dataset. Two primary evaluation metrics were used: the coefficient of determination (R^2) to quantify the variance explained by the model in predicting absolute expression values, and Spearman's rank correlation coefficient to measure the concordance between predicted and actual expression rankings.

Download of genome sequence and small RNA annotation

The reference genomes for mouse (mm10), human (hg38), and crab-eating monkey (macFas5) were downloaded from the UCSC Genome Browser (https://hgdownload.soe.ucsc.edu/). Genome annotations for crab-eating monkeys were obtained from UCSC, while annotations for mice and human genome annotations were downloaded from Gencode (https://www.gencodegenes.org/). Small RNA annotations for humans and mice were sourced as follows: miRNA annotations were downloaded from miRBase (release 22, https://mirbase.org/download/) and

retained only unique sequences. tRNA annotations were obtained from Ensembl (release 110, https://www.ensembl.org/biomart/martview/) and GtRNAdb (release 21, http://gtrnadb.ucsc.edu/index.html), with duplicate entries removed. rRNA annotations were retrieved from Ensembl and NCBI (https://www.ncbi.nlm.nih.gov/nucleotide/), and duplicates were similarly removed. piRNA annotations were sourced from the piRBase gold standard set (release v3.0, http://bigdata.ibp.ac.cn/piRBase/). Annotations for snRNA, scRNA, snoRNA, scaRNA, YRNA, mRNA, and lincRNA were downloaded from Ensembl. Small RNA annotations for crab-eating monkeys were sourced as follows: miRNA annotations from miRBase for rhesus macaques, with unique sequences retained. Annotations for rRNA, tRNA, snRNA, and scRNA from UCSC (https://hgdownload.soe.ucsc.edu/goldenPath/macFas5/database/rmsk.txt). Additionally, to comprehensively classify small RNAs derived from functional RNAs, we combined the annotated functional RNA sequences from the rhesus macaque genome with corresponding annotations from the crab-eating monkey genome. Annotations for rhesus macaques were retrieved from NCBI (https://www.ncbi.nlm.nih.gov/).

Webserver and database implementation

To create an efficient and engaging web interface for the SmallQuant database, we employed the following tools: Django (v4.2.1) for web development, Bootstrap (v3.3.7) for responsive design, jQuery (v3.2.1) for dynamic interactions, Python 3.8 for backend processing, and ECharts for interactive data visualization. Data management and retrieval were conducted using MySQL (v8.0.35).

DATA AVAILABILITY

The deep-sequencing data have been deposited at the National Center for Biotechnology Information NCBI Gene Expression Omnibus (http://www.ncbi.nlm.nih.gov/geo/) database under accession number GSE279145. All other data supporting the findings of this study are available from the corresponding authors upon reasonable request. The following publicly available

datasets were used: K562 AQ-seq data from GSE158025; K562 Truseq data from GSE102497; HCT116 AQ-seq data from GSE230544; HCT116 Truseq data from GSE180613 and GSE189908; HEK293T and Hela AQ-seq data from GSE123627; HEK293T and Hela Truseq data from GSE57295; HEK293T IsoSeek data from PRJNA867189; mouse liver and brain Truseq data from GSE227578.

AUTHOR CONTRIBUTIONS

L.W. and H.Z. conceived and designed the study. Y.Z. and H.Z. conceived and developed the methodology of qMap-seq. B.X., R.Z., W.X., and Y.Z. collected the cells and tissues. B.X., R.Z., and Y.Z. isolated all the RNAs. Y.Z. generated all sncRNA-seq libraries. W.X. designed spike-ins and performed computational analyses. W.X., H.Z., and Y.Z. interpreted the data. W.X., H.Z., L.W., and Y.Z. wrote the manuscript.

ACKNOWLEDGEMENTS

We are grateful to Jin Ren and Xinming Qi for providing Crab-eating monkey tissues. We thank all members of L. Wu's laboratories for their discussion and comments on this project; Y. Xu for his assistance with high-performance computing; and staff at the HPC storage and network service platform of SIBCB for supplying the computing resources. Fig. 2A and Fig. 6A are created with BioRender.com released under a Creative Commons Attribution-NonCommercial-NoDerivs 4.0 International license.

FUNDING

This work was supported by the National Key R&D Program of China (2022YFA1303301), the Strategic Priority Research Program of the Chinese Academy of Sciences (XDB0570000), and the National Key R&D Program of China (2021YFA1100201) to Ligang Wu; the National Natural Science Foundation of China (32200696) and the Youth Innovation Promotion Association CAS to H.Z.

CONFLICT OF INTEREST

The authors declare no competing interests.

REFERENCE

1. Bartel, D.P., *Metazoan MicroRNAs.* Cell, 2018. **173**(1): p. 20-51.
2. Lu, T.X. and M.E. Rothenberg, *MicroRNA.* J Allergy Clin Immunol, 2018. **141**(4): p. 1202-1207.
3. Cech, T.R. and J.A. Steitz, *The noncoding RNA revolution-trashing old rules to forge new ones.* Cell, 2014. **157**(1): p. 77-94.
4. Li, X., J. Peng, and C. Yi, *The epitranscriptome of small non-coding RNAs.* Noncoding RNA Res, 2021. **6**(4): p. 167-173.
5. Esteller, M., *Non-coding RNAs in human disease.* Nature Reviews Genetics, 2011. **12**(12): p. 861-874.
6. Shang, R., et al., *microRNAs in action: biogenesis, function and regulation.* Nat Rev Genet, 2023. **24**(12): p. 816-833.
7. Diener, C., A. Keller, and E. Meese, *The miRNA-target interactions: An underestimated intricacy.* Nucleic Acids Res, 2024. **52**(4): p. 1544-1557.
8. Stefani, G. and F.J. Slack, *Small non-coding RNAs in animal development.* Nature Reviews Molecular Cell Biology, 2008. **9**(3): p. 219-230.
9. Hu, J.F., et al., *Quantitative mapping of the cellular small RNA landscape with AQRNA-seq.* Nat Biotechnol, 2021. **39**(8): p. 978-988.
10. Wang, H., et al., *CPA-seq reveals small ncRNAs with methylated nucleosides and diverse termini.* Cell Discov, 2021. **7**(1): p. 25.
11. Park, J., et al., *tRNA-Derived Small RNAs: Novel Epigenetic Regulators.* Cancers (Basel), 2020. **12**(10).
12. Chen, Q., et al., *Origins and evolving functionalities of tRNA-derived small RNAs.* Trends Biochem Sci, 2021. **46**(10): p. 790-804.
13. Shi, J., et al., *PANDORA-seq expands the repertoire of regulatory small RNAs by overcoming RNA modifications.* Nat Cell Biol, 2021. **23**(4): p. 424-436.
14. Chu, C., et al., *A sequence of 28S rRNA-derived small RNAs is enriched in mature sperm and various somatic tissues and possibly associates with inflammation.* J Mol Cell Biol, 2017. **9**(3): p. 256-259.
15. Dard-Dascot, C., et al., *Systematic comparison of small RNA library preparation protocols for next-generation sequencing.* BMC Genomics, 2018. **19**(1): p. 118.
16. Yang, Q., et al., *Single-cell CAS-seq reveals a class of short PIWI-interacting RNAs in human oocytes.* Nat Commun, 2019. **10**(1): p. 3389.
17. Maguire, S. and S. Guan, *Rolling circle reverse transcription enables high fidelity nanopore sequencing of small RNA.* PLoS One, 2022. **17**(10): p. e0275471.
18. Barberan-Soler, S., et al., *Decreasing miRNA sequencing bias using a single adapter and circularization approach.* Genome Biol, 2018. **19**(1): p. 105.
19. Sterling, C.H., I. Veksler-Lublinsky, and V. Ambros, *An efficient and sensitive method for preparing cDNA libraries from scarce biological samples.* Nucleic Acids Res, 2015. **43**(1): p. e1.
20. Masotti, A., et al., *Quantification of small non-coding RNAs allows an accurate*

comparison of miRNA expression profiles. J Biomed Biotechnol, 2009. **2009**: p. 659028.

21. Zhou, L., et al., *Small RNA transcriptome investigation based on next-generation sequencing technology.* J Genet Genomics, 2011. **38**(11): p. 505-13.
22. Khamina, K., et al., *A MicroRNA Next-Generation-Sequencing Discovery Assay (miND) for Genome-Scale Analysis and Absolute Quantitation of Circulating MicroRNA Biomarkers.* Int J Mol Sci, 2022. **23**(3).
23. Pfeffer, S., M. Lagos-Quintana, and T. Tuschl, *Cloning of small RNA molecules.* Curr Protoc Mol Biol, 2005. **Chapter 26**(1): p. Unit 26 4.
24. Elbashir, S.M., W. Lendeckel, and T. Tuschl, *RNA interference is mediated by 21- and 22-nucleotide RNAs.* Genes Dev, 2001. **15**(2): p. 188-200.
25. Viollet, S., et al., *T4 RNA ligase 2 truncated active site mutants: improved tools for RNA analysis.* BMC Biotechnol, 2011. **11**: p. 72.
26. Lau, N.C., et al., *An abundant class of tiny RNAs with probable regulatory roles in Caenorhabditis elegans.* Science, 2001. **294**(5543): p. 858-62.
27. Git, A., et al., *Systematic comparison of microarray profiling, real-time PCR, and next-generation sequencing technologies for measuring differential microRNA expression.* RNA, 2010. **16**(5): p. 991-1006.
28. Linsen, S.E., et al., *Limitations and possibilities of small RNA digital gene expression profiling.* Nat Methods, 2009. **6**(7): p. 474-6.
29. Sorefan, K., et al., *Reducing ligation bias of small RNAs in libraries for next generation sequencing.* Silence, 2012. **3**(1): p. 4.
30. Zhuang, F., et al., *Structural bias in T4 RNA ligase-mediated 3'-adapter ligation.* Nucleic Acids Res, 2012. **40**(7): p. e54.
31. Raabe, C.A., et al., *Biases in small RNA deep sequencing data.* Nucleic Acids Res, 2014. **42**(3): p. 1414-26.
32. Kim, H., et al., *Bias-minimized quantification of microRNA reveals widespread alternative processing and 3' end modification.* Nucleic Acids Res, 2019. **47**(5): p. 2630-2640.
33. van Eijndhoven, M.A.J., et al., *IsoSeek for unbiased and UMI-informed sequencing of miRNAs from low input samples at single-nucleotide resolution.* STAR Protoc, 2023. **4**(4): p. 102645.
34. Belair, C.D., et al., *High-throughput, Efficient, and Unbiased Capture of Small RNAs from Low-input Samples for Sequencing.* Sci Rep, 2019. **9**(1): p. 2262.
35. Giraldez, M.D., et al., *Comprehensive multi-center assessment of small RNA-seq methods for quantitative miRNA profiling.* Nature Biotechnology, 2018. **36**(8): p. 746-757.
36. Nandakumar, J. and S. Shuman, *How an RNA ligase discriminates RNA versus DNA damage.* Mol Cell, 2004. **16**(2): p. 211-21.
37. Munafo, D.B. and G.B. Robb, *Optimization of enzymatic reaction conditions for generating representative pools of cDNA from small RNA.* RNA, 2010. **16**(12): p. 2537-52.
38. van Dijk, E.L., E. Eleftheriou, and C. Thermes, *Improving Small RNA-seq: Less Bias and Better Detection of 2'-O-Methyl RNAs.* J Vis Exp, 2019(151).

39. Maguire, S., G.J.S. Lohman, and S. Guan, *A low-bias and sensitive small RNA library preparation method using randomized splint ligation.* Nucleic Acids Res, 2020. **48**(14): p. e80.
40. Cui, Y., et al., *miRNA dosage control in development and human disease.* Trends Cell Biol, 2024. **34**(1): p. 31-47.
41. Ameres, S.L. and P.D. Zamore, *Diversifying microRNA sequence and function.* Nat Rev Mol Cell Biol, 2013. **14**(8): p. 475-88.
42. Kozomara, A., M. Birgaoanu, and S. Griffiths-Jones, *miRBase: from microRNA sequences to function.* Nucleic Acids Res, 2019. **47**(D1): p. D155-D162.
43. Fromm, B., et al., *MirGeneDB 2.1: toward a complete sampling of all major animal phyla.* Nucleic Acids Res, 2022. **50**(D1): p. D204-D210.
44. Panwar, B., G.S. Omenn, and Y. Guan, *miRmine: a database of human miRNA expression profiles.* Bioinformatics, 2017. **33**(10): p. 1554-1560.
45. Kavakiotis, I., et al., *DIANA-miTED: a microRNA tissue expression database.* Nucleic Acids Res, 2022. **50**(D1): p. D1055-D1061.
46. Isakova, A., et al., *A mouse tissue atlas of small noncoding RNA.* Proc Natl Acad Sci U S A, 2020. **117**(41): p. 25634-25645.
47. Landgraf, P., et al., *A mammalian microRNA expression atlas based on small RNA library sequencing.* Cell, 2007. **129**(7): p. 1401-14.
48. Xu, P., et al., *An improved protocol for small RNA library construction using High Definition adapters.* Methods in Next Generation Sequencing, 2015. **2**(1).
49. Clement, K., et al., *AmpUMI: design and analysis of unique molecular identifiers for deep amplicon sequencing.* Bioinformatics, 2018. **34**(13): p. i202-i210.
50. Fu, Y., et al., *Elimination of PCR duplicates in RNA-seq and small RNA-seq using unique molecular identifiers.* BMC Genomics, 2018. **19**(1): p. 531.
51. Faridani, O.R., et al., *Single-cell sequencing of the small-RNA transcriptome.* Nature Biotechnology, 2016. **34**(12): p. 1264-1266.
52. Bissels, U., et al., *Absolute quantification of microRNAs by using a universal reference.* Rna, 2009. **15**(12): p. 2375-2384.
53. Hafner, M., et al., *RNA-ligase-dependent biases in miRNA representation in deep-sequenced small RNA cDNA libraries.* RNA, 2011. **17**(9): p. 1697-712.
54. Jayaprakash, A.D., et al., *Identification and remediation of biases in the activity of RNA ligases in small-RNA deep sequencing.* Nucleic Acids Res, 2011. **39**(21): p. e141.
55. Fuchs, R.T., et al., *Bias in ligation-based small RNA sequencing library construction is determined by adaptor and RNA structure.* PLoS One, 2015. **10**(5): p. e0126049.
56. Kim, H., et al., *A Mechanism for microRNA Arm Switching Regulated by Uridylation.* Mol Cell, 2020. **78**(6): p. 1224-1236 e5.
57. Srinivasan, G., et al., *MiR223-3p promotes synthetic lethality in BRCA1-deficient cancers.* Proc Natl Acad Sci U S A, 2019. **116**(35): p. 17438-17443.
58. Ohanian, M., et al., *A heterozygous variant in the human cardiac miR-133 gene, MIR133A2, alters miRNA duplex processing and strand abundance.* BMC Genet, 2013. **14**: p. 18.
59. Suzuki, H.I., et al., *Small-RNA asymmetry is directly driven by mammalian Argonautes.* Nat Struct Mol Biol, 2015. **22**(7): p. 512-21.

60. Mathelier, A. and A. Carbone, *Large scale chromosomal mapping of human microRNA structural clusters.* Nucleic Acids Res, 2013. **41**(8): p. 4392-408.
61. Gregorova, J., P. Vychytilova-Faltejskova, and S. Sevcikova, *Epigenetic Regulation of MicroRNA Clusters and Families during Tumor Development.* Cancers (Basel), 2021. **13**(6).
62. Bartel, D.P., *MicroRNAs: target recognition and regulatory functions.* Cell, 2009. **136**(2): p. 215-33.
63. Medley, J.C., G. Panzade, and A.Y. Zinovyeva, *microRNA strand selection: Unwinding the rules.* Wiley Interdiscip Rev RNA, 2021. **12**(3): p. e1627.
64. Kilikevicius, A., G. Meister, and D.R. Corey, *Reexamining assumptions about miRNA-guided gene silencing.* Nucleic Acids Res, 2022. **50**(2): p. 617-634.
65. Androsavich, J.R., et al., *Disease-linked microRNA-21 exhibits drastically reduced mRNA binding and silencing activity in healthy mouse liver.* RNA, 2012. **18**(8): p. 1510-26.
66. Roush, S. and F.J. Slack, *The let-7 family of microRNAs.* Trends Cell Biol, 2008. **18**(10): p. 505-16.
67. Kowarsch, A., et al., *miTALOS: analyzing the tissue-specific regulation of signaling pathways by human and mouse microRNAs.* RNA, 2011. **17**(5): p. 809-19.
68. Ludwig, N., et al., *Distribution of miRNA expression across human tissues.* Nucleic Acids Res, 2016. **44**(8): p. 3865-77.
69. Keller, A., et al., *miRNATissueAtlas2: an update to the human miRNA tissue atlas.* Nucleic Acids Res, 2022. **50**(D1): p. D211-D221.
70. Guo, Z., et al., *Genome-wide survey of tissue-specific microRNA and transcription factor regulatory networks in 12 tissues.* Sci Rep, 2014. **4**: p. 5150.
71. Lagos-Quintana, M., et al., *Identification of tissue-specific microRNAs from mouse.* Curr Biol, 2002. **12**(9): p. 735-9.
72. Zhou, B., et al., *miR-150, a microRNA expressed in mature B and T cells, blocks early B cell development when expressed prematurely.* Proc Natl Acad Sci U S A, 2007. **104**(17): p. 7080-5.
73. Wang, T., F. Wu, and D. Yu, *miR-144/451 in hematopoiesis and beyond.* ExRNA, 2019. **1**(1).
74. Giraldez, M.D., et al., *Comprehensive multi-center assessment of small RNA-seq methods for quantitative miRNA profiling.* Nat Biotechnol, 2018. **36**(8): p. 746-757.
75. Lai, H., N. Feng, and Q. Zhai, *Discovery of the major 15–30 nt mammalian small RNAs, their biogenesis and function.* Nature Communications, 2023. **14**(1): p. 5796.
76. Wang, H., et al., *CPA-seq reveals small ncRNAs with methylated nucleosides and diverse termini.* Cell Discovery, 2021. **7**(1): p. 25.
77. Shi, J., et al., *PANDORA-seq expands the repertoire of regulatory small RNAs by overcoming RNA modifications.* Nature Cell Biology, 2021. **23**(4): p. 424-436.
78. Hu, J.F., et al., *Quantitative mapping of the cellular small RNA landscape with AQRNA-seq.* Nature Biotechnology, 2021. **39**(8): p. 978-988.

Figure legends:

Figure 1: qMap-seq significantly reduces ligation bias and achieves accurate quantification.

(A) Schematic representation of the qMap-seq library preparation workflow. **(B)** The CV of the distribution of 30 (sequences with 2'-OH or 2'-Ome at the 3' ends) or 7 (sequence with 2'-Ome at the 3' ends) equimolar spike-ins, using total HEK293 cellular RNA as background, is shown in the box plots. In these plots, the center line represents the median, while the box edges correspond to the 25th and 75th percentiles. The whiskers extend to the minimum and maximum values. The biological replicates for these experiments were n = 2 for Truseq and n = 4 for qMap-seq. **(C)** Pie charts illustrating the proportion of 30 equimolar spike-ins detected by TruSeq and qMap-seq in representative samples. **(D)** The correlations between the ground truth and predicted abundances of ratiometric spike-ins in various samples are illustrated, with blue points representing unmodified sequences and red points indicating sequences with 2'-Ome at the 3' ends. **(E)** Scatter plots illustrating the correlation between the ground truth and predicted abundances of additional external spike-ins. **(F)** Scatter plot illustrating the correlation between the predicted abundances of the selected miRNA as measured by qMap-seq and qRT-PCR, with different colors representing distinct cell lines. Each cell line is represented by three to four biological replicates. All p-values were calculated using two-tailed Student's t-tests.

Figure 2: Overview of miRNA expression across various tissues and cell lines.

(A) Tissues and cell lines collected for this study. **(B)** Data analysis workflow for this study. **(C)** Proportions of various small RNA types within all small RNA libraries.

Figure 3: Species and quantification of miRNAs across cell lines and tissues.

(A-B) Box plots showing the number of detected miRNA species across various cell lines **(A)** and tissues **(B)**, with 1.5 million mapped molecules from each sample used for analysis. **(C-E)** Box plots illustrating the absolute abundance of miRNA in various

cell lines **(C)** and tissues **(D-E)**. In these plots, the center line represents the median value, the box borders represent the upper and lower quartiles (25th and 75th percentiles, respectively), and the ends of the top and bottom whiskers represent maximum and minimum scores, respectively. Biological replicates: n = 2 (mouse-ovary, mouse-testis) or n = 3 (Caco2, mouse-breast, monkey-rectum, monkey-stomach) or n = 4 (remaining samples).

Figure 4: Re-assessment of miRNA strand preference.

(A) Proportions of the 5' and 3' arms of representative miRNAs in various tissues and cell lines, as measured by qMap-seq. miRNAs in red bold indicate that their strand preferences have been previously validated. **(B)** A table showing representative miRNAs with previously validated strand preferences and those identified by our datasets. **(C)** Comparison of 5p/3p ratios for the top 100 miRNAs identified by our datasets, AQ-seq and Truseq in HCT116 or HEK293T cell lines. Statistical significance was assessed using two-tailed Student's t-tests. **(D)** Comparison of miRNA strand ratios predicted by the model with those obtained from our datasets (left), AQ-seq (middle), and TruSeq (right) in HEK293T, HCT116, and K562 cells. **(E)** Strand preference of expressed miRNAs across species. miRNAs with over 75% expression from the 5p arm are classified as 5p, those with less than 25% from the 5p arm as 3p, and those in between are categorized as no preference. **(F)** 5p/3p ratios of representative miRNAs across various cell lines measured by our datasets and TruSeq. Annotated strand preferences from miRBase are displayed below, with bold text highlighting annotations that are inconsistent with our datasets.

Figure 5: The expression of miRNA families across cell lines and tissues.

(A) Expression patterns of the top 30 miRNA families in cell lines based on our datasets and the DIANA-miTED database. Circle size represents the proportion of miRNA family expression relative to total miRNA families. **(B)** The representative miRNA families whose expression was overrepresented (up) or underestimated (bottom) in the DIANA-miTED database compared to our datasets. **(C)** Expression

patterns of the top 30 miRNA families in mouse and monkey tissues. Circle size represents the absolute abundance of each miRNA family. **(D)** Confusion matrix of miRNA families with a tissue-specificity index (TSI) greater than 0.85. Numbers within the bubbles indicate the number of overlapping tissue-specific miRNA families between our datasets and MirGeneDB across various species. Numbers in parentheses on the axes denote the total number of tissue-specific miRNA families identified in each tissue using our datasets (x-axis) and MirGeneDB (y-axis). **(E)** The absolute abundance of tissue-specific miRNA families uniquely identified by MirGeneDB (MirGeneDB unique) or common by MirGeneDB and our datasets (Shared). **(F)** Expression levels of tissue-specific miRNA families uniquely identified by our datasets in the MirGeneDB and our datasets. Statistical significance was assessed using two-tailed Student's t-tests. Data in (A) and (C) are presented as mean values.

Figure 6: Machine learning-based correction of sequencing bias.

(A) Schematic workflow of the predictive model, trained on paired datasets generated using NEBNext Small RNA Library Prep (NEBNext) and qMap-seq. **(B)** Concordance between qMap-seq measured and model-predicted miRNA expression values. **(C-D)** Comparison of miRNA expression rankings before (left) and after (right) bias correction, relative to qMap-seq measurements in both test **(C)** and validation sets **(D)**.

Figure 7: Snapshot depicting the SmallQuant interface.

Users can view an overview of database statistics from the home interface. The Database interface offers a range of filtering options to refine absolute quantitative information or rankings for sncRNAs of interest, including species, tissue or cell types, and small RNA types. The miRNA search interface provides access to quantitative data and strand preference information for specified miRNAs across various tissues or cell lines. Additionally, the snRNA profile interface displays the proportions of

different sncRNAs expressed in various tissues and cell lines, along with absolute quantitative information for total miRNA.

Supplementary Figure 1: Establishment of the qMap-seq method

(A) Histogram illustrates the collision ratios predicted by the AmpUMI model for UMIs with varying random base lengths. The x-axis indicates the UMI random base lengths, while the y-axis displays the predicted collision ratios.

(B) Schematic illustrating the design, selection, and pooling process for equimolar and ratiometric spike-ins.

(C) Pie charts showing the proportion of 30 equimolar spike-ins detected under different concentrations of 3' and 5' adapters.

(D) Histogram showing the dropping and mapping ratios of libraries at varying concentrations of adapters.

(E) Dual line graph illustrating the CVs of equimolar spike-ins and the number of detected miRNA species across different adapter concentrations. The x-axis represents adapter concentrations, while the left y-axis displays the CVs of equimolar spike-ins, and the right y-axis presents the number of detected miRNA species.

(F) Comparison of the efficiency of Lambda exonuclease and RecJ exonuclease in depleting excess 3' adapters. In a typical reaction, more than 30 U RecJ or 1.25 U Lambda exonuclease can efficiently remove excess 3’ adapter, resulting in the successful miRNA library construction (lines 1, 2, and 6). However, if the concentration of RecJ exonuclease is below 30 U, excess 3’ adapters can ligate to 5’ adapters, resulting in a large amount of byproducts (lines 3 and 4, highlighted by the blue frame). Additionally, the high efficiency of Lambda exonuclease in depleting 3’ adapters require the annealing of 3’ adapters and RTP (lines 5 vs. line 6).

(G) The CV of the distribution of 23 (sequences with 2’-OH) equimolar spike-ins, using total HEK293 cellular RNA as background, is shown in the box plots. In these plots, the center line represents the median, while the box edges correspond to the 25th and 75th percentiles. The whiskers extend to the minimum and maximum values. The biological replicates for these experiments were n = 2 for Truseq, n = 4 for qMap-seq

and n = 6 for AQ-seq.

(H) Relative abundance of non-methylated spike-ins compared to their terminal methylated counterparts. This analysis was performed based on the expression of seven pairs of spike-ins from equimolar spike-in pools spiked into 100 ng HEK293 total RNAs. Each pair consisted of one non-methylated and one terminally methylated RNA molecule with nearly identical sequences, differing by only two nucleotides. A higher relative abundance indicates more efficient ligation of the non-methylated spike-in compared to its methylated counterpart. The biological replicates for these experiments were n = 2 for TruSeq and qMap-seq.

(I) Relative nucleotide composition of the top 10,000 piRNAs in TruSeq and qMap libraries from mouse testis.

(J) Pearson correlation of miRNA expression profiles from libraries at different dilutions, compared to the profile from 1 µg of input RNA.

(K) Proportion of miRNA species detected from libraries at different dilutions, compared to the miRNA species detected from 1 µg of input RNA.

Data in (C), (D), (E), (J), and (K) represent two biological replicates. Data represent mean ± s.e.m.

Supplementary Figure 2: The data quality of qMap-seq libraries from cell lines and tissues

(A) Violin plot showing the distribution of mapped reads across all small RNA libraries.

(B-D) t-SNE projection based on miRNA expression in cell lines**(B)**, mouse (**C**), and monkey (**D**) tissues, with each cell line or tissue represented by three to four biological replicates.

(E) Represented examples demonstrating the quantification precision achieved by qMap-seq. The standard curve for each library were established using ratiometric spike-ins with known absolute molecule numbers. Four additional spike-ins, each with varying but known absolute molecule counts, were plotted to evaluate the precision of these standard curves. The x-axis represents the sequencing molecule numbers of each spike-ins, and the y-axis shows their corresponding absolute molecule numbers.

The R^2 values indicate the fit of these standard curves. Blue points represent the 30 ratiometric spike-ins, and red points represent the four additional spike-ins.

(F) Assessment of qMap-seq's quantification accuracy. Predicted molecule counts of four spike-ins in each sample were calculated from standard curves and plotted against their actual molecule counts. The strong correlation between predicted and ground truth values demonstrates that qMap-seq can accurately quantify the molecule counts of sncRNAs.

(G) Assessment of miRNA family expression stability within each cell line. Bars indicate the CV of representative miRNA family expression levels across biological replicates. Biological replicates: n = 3 (Caco2) or n = 4 (remaining samples).

Supplementary Figure 3: Predicted heterodimer structures formed between miRNAs and fixed or random 5' adapters

(A-B) Predicted heterodimer structures formed between underestimated **(A)** or overestimated miRNAs **(B)** and fixed 5' RNA adapters used in the Truseq protocol.

(C) Predicted heterodimer structures formed between these underestimated miRNAs, as shown in (A), and random 5' adapters used in the qMap-seq protocol.

Three representative structures are shown on the left. Sequences with red background indicate the miRNAs, while sequences with green background represent the 5' RNA adapters. Statistical results for all miRNAs are summarized in the table on the right.

Supplementary Figure 4: Re-evaluation of miRNA family expression

(A-B) Expression patterns of the top 30 miRNA families in mice **(A)** and monkeys **(B)** based on our datasets or the MirGeneDB database. Circle size represents the proportion of miRNA family expression relative to total miRNA families.

(C-D) Comparison of overestimated or underestimated representative miRNA family expression between our datasets and the MirGeneDB database for mouse **(C)** and monkey tissues **(D)**. Significance was assessed using two-tailed Student's t-tests.

Supplementary Figure 5: Tissue-specific miRNA families are highly conserved between mice and monkeys

(A) TSI distribution of highly expressed miRNA families (the proportion of miRNA family expression relative to total miRNA families >1%) in monkey and mouse tissues. **(B)** Confusion matrix of miRNA families with a TSI greater than 0.85. Numbers inside the bubbles indicate the number of overlapping tissue-specific miRNA families between monkey and mouse tissues. Numbers in parentheses along the x- and y-axes represent the tissue-specific miRNA families identified in monkeys and mice, respectively.

Tables:

Table 1. Tissue-specific miRNA families identified in monkey and mouse tissues using SmRNAQuant datasets.

Tissues	Monkey	Mouse	Overlap
Blood	miR-144, miR-451, miR-19, miR-142, miR-101	miR-144, miR-451, miR-19, miR-142, miR-15, miR-17	4
Brain	miR-124, miR-9, miR-132, miR-137, miR-128	miR-124, miR-9, miR-132, miR-137, miR-128, miR-218, miR-154, miR-127	5
Erythrocyte	miR-486, miR-92, miR-191, miR-17, miR-15, let-7	miR-486, miR-92	2
Heart	miR-499, miR-1, miR-133	miR-499, miR-1, miR-133	3
Leukocyte	miR-150	miR-150	1
Liver	miR-122	miR-122	1
Muscle	miR-133, miR-1, miR-499	miR-133, miR-1	2
Pancreas	miR-216, miR-217, miR-459, miR-375	miR-216, miR-217, miR-459	3
Skin	miR-203, miR-205	miR-203, miR-205	2
Rectum	-	miR-194	0
Colon	-	miR-192, miR-375	0
Thymus	-	miR-181	0

Table 2. Tissue-specific miRNA families identified in monkey tissues using SmRNAQuant and MirGeneDB.

Tissues	SmRNAQuant	MirGeneDB	Overlap
Brain	miR-124, miR-128, miR-129, miR-132, miR-137, miR-149, miR-9	miR-124, miR-127, miR-128, miR-129, miR-132, miR-137, miR-138, miR-149, miR-218, miR-7, miR-9	7
Heart	miR-499, miR-1, miR-133	miR-499, miR-1, miR-133, miR-378	3
Kidney	miR-190, miR-204, miR-8	miR-190	1
Liver	miR-122, miR-192, miR-194	miR-122, miR-148, miR-192, miR-194	3
Muscle	miR-1, miR-133, miR-499	miR-1, miR-133, miR-378	2
Spleen	miR-142, miR-146, miR-150, miR-335	miR-142, miR-150	2
Thymus	miR-205	miR-155, miR-205	1

Table 3. Tissue-specific miRNA families identified in mouse tissues using SmRNAQuant and MirGeneDB.

Tissues	SmRNAQuant	MirGeneDB	Overlap
Brain	miR-124, miR-127, miR-128, miR-132, miR-9	miR-124, miR-127, miR-128, miR-132, miR-9, miR-126, miR-135, miR-15, miR-23	5
Heart	miR-499, miR-1, miR-133	miR-1, miR-499	2
Intestine	miR-192, miR-194, miR-375	miR-145, miR-192, miR-194, miR-459, miR-8	2
Liver	miR-122	miR-122	1
Muscle	miR-1, miR-133	miR-133, miR-22	1
Pancreas	miR-216, miR-459	miR-148, miR-216, miR-375	1
Skin	miR-203, miR-205	miR-203, miR-205	2
Spleen	miR-142, miR-150	miR-142, miR-143, miR-146, miR-150, miR-19, miR-21, miR-451	2
Testis	miR-202, miR-34, miR-506	miR-202, miR-34, miR-506	3
Ovary	miR-135, miR-202	-	0

Supplementary Table 1: Methods for cell lysis of each tissue

Mouse		Crab-eating monkey	
Tissue	**Method**	**Tissue**	**Method**
lung	magnetic beads	lung	liquid nitrogen
breast	liquid nitrogen	breast	liquid nitrogen
colon	magnetic beads	colon	magnetic beads
rectum	magnetic beads	rectum	magnetic beads
kidney	magnetic beads	kidney	magnetic beads
brain	magnetic beads	brain	liquid nitrogen
skin	liquid nitrogen	skin	liquid nitrogen
liver	magnetic beads	liver	magnetic beads
stomach	magnetic beads	stomach	magnetic beads
spleen	magnetic beads	spleen	magnetic beads
pancreas	liquid nitrogen	pancreas	liquid nitrogen
heart	magnetic beads	heart	magnetic beads
thymus	magnetic beads	thymus	magnetic beads
muscle	magnetic beads	muscle	magnetic beads
adipose	magnetic beads	adipose	magnetic beads
testis	magnetic beads	-	-
ovary	magnetic beads	-	-

Supplementary Table 2: The sequences of adapters, along with the sequences and specific mixing ratios of EM and RM spike-ins

Spike-in or adapter	Sequence	Length	EM	RM
1	AACUUCUCACUAUCUUCGGGCAUACAUC	28	40 μM	10 μM
14	GUCGAAGAUAAUUACCGGAG	20	40 μM	10 μM
20	UUACAUUCCUCUGAAAAACGGCC	23	40 μM	10 μM
2m	GCCAUCAUUACCAAUACCGmA	20	40 μM	2.5 μM
21	AACUUCAGGGUCAGCUUGCCG	21	40 μM	2.5 μM
22	CCUGGACUAGUCGUCAGCAUU	21	40 μM	2.5 μM
6	UCUAUGCCAAACCGACCUAGCCG	23	40 μM	625 nM
7m	AGAUCACGAUGUACUUUCCCCGCUmU	25	40 μM	625 nM
23	UACCCGUAAUCUUCAUAAUCCGAG	24	40 μM	625 nM
8	ACCUGCCCCCAAUAUCGUGAU	21	40 μM	156 nM
10m	UCCCAACCCUAACCGAAGCGAUUAGmU	26	40 μM	156 nM
17	GAGUCUACGUAACCACAUAG	20	40 μM	156 nM
9	GGCUCCCUAACAAUACGACU	20	40 μM	39 nM
18	UACACAAAGAUGUCAGCCAGAU	22	40 μM	39 nM
20m	UUACAUUCGACUGAAAAACGGCmC	23	40 μM	39 nM
10	UCCCAACCGAAACCGAAGCGAUUAGU	26	40 μM	9.8 nM
19	UGAUCCUAAAAAUUCGCGCCUCACUCCAC	29	40 μM	9.8 nM
21m	AACUUCAGGGGAAGCUUGCCmG	21	40 μM	9.8 nM
4	CGAGGGCAAGUAAAUAGUAGGUUA	24	40 μM	2.4 nM
11	UCUGCCGUUUGAUGAUAC	20	40 μM	2.4 nM

	UU			
22m	CCUGGACUAGUCGUCAGUGUmU	21	40 μM	2.4 nM
7	AGAUCACGAACUACUUUCCCCGCUU	25	40 μM	610 pM
15	UCCCGCAACUCAACUACCUCCA	22	40 μM	610 pM
23m	UACCCGUAAUAGUCAUAAUCCGAmG	24	40 μM	610 pM
2	GCCAUCAUAUCCAAUACCGA	20	40 μM	153 pM
5	ACCAGGCGUUCGAUUCAAAAC	21	40 μM	153 pM
12	UACCCUCAGAUUCCUCCCCGCGUUC	25	40 μM	153 pM
3	AAGUUUACCCGCGGUUUAAA	20	40 μM	38 pM
13	UUCGUCCUAUAAGAGUUGUG	20	40 μM	38 pM
16	AUUAUACAUUUGCGUACCCCUUCCA	25	40 μM	38 pM
3' randomized adapter	/rApp/(N:25252525)(N)(N)(N)TGGAATTCTCGGGTGCCAAGG/ddC/	-	-	-
5' randomized adapter	rGrUrUrCrArGrArGrUrUrCrUrArCrArGrUrCrCrGrArCrGrArUrCrNrNrNrCrGrAr(N:25252525)r(N)r(N)r(N)	-	-	-

Supplementary Table 3: The sequence of qRT-PCR primer

Name	Sequence	Length	RT primer
hsa-mir-221-3p	AGCTACATTGTCTGCTGGGTTTC	23	GTCGTATCCAGTGCAGGGTCCGAGGTATTCGCACTGGATACGACGAAACCCAGC

Supplementary Datasets:

Supplementary Dataset 1. Tissues and cell lines commonly used in previous miRNA studies

Supplementary Dataset 2. miRNA species and absolute expression levels across different cell lines and tissues in this study

Supplementary Dataset 3. Over- and underestimated miRNAs in cell lines or tissues

Supplementary Dataset 4. The miRNA log2 (5p/3p) obtained from different miRNA in cell lines and tissues

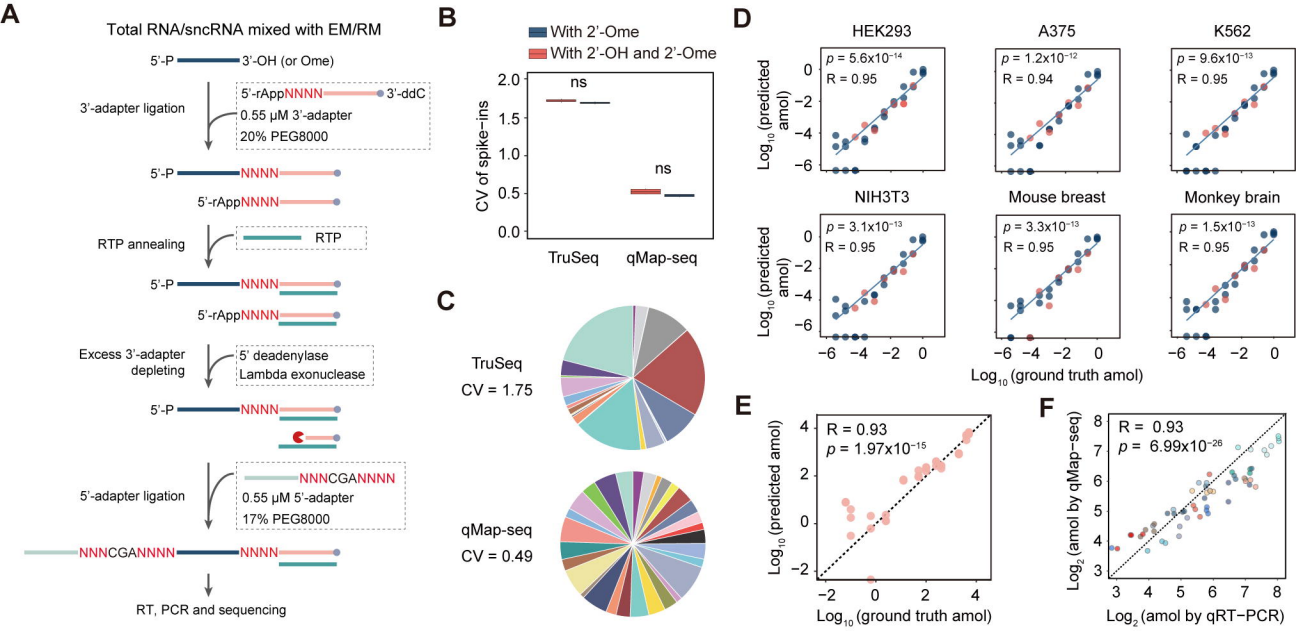
A
Total RNA/sncRNA mixed with EM/RM
5'-P
3'-OH (or Ome)
3'-adapter ligation
5'-rAppNNNN
3'-ddC
0.55 μM 3'-adapter
20% PEG8000
NNNN
5'-rAppNNNN
RTP annealing
RTP
Excess 3'-adapter depleting
5' deadenylase
Lambda exonuclease
5'-adapter ligation
NNNCGANNNN
0.55 μM 5'-adapter
17% PEG8000
RT, PCR and sequencing
B
With 2'-Ome
With 2'-OH and 2'-Ome
CV of spike-ins
ns
TruSeq
qMap-seq
C
TruSeq
CV = 1.75
qMap-seq
CV = 0.49
D
HEK293
A375
K562
NIH3T3
Mouse breast
Monkey brain
R = 0.95
R = 0.94
Log10 (predicted amol)
Log10 (ground truth amol)
E
R = 0.93
Log10 (predicted amol)
Log10 (ground truth amol)
F
R = 0.93
Log2 (amol by qMap-seq)
Log2 (amol by qRT-PCR)

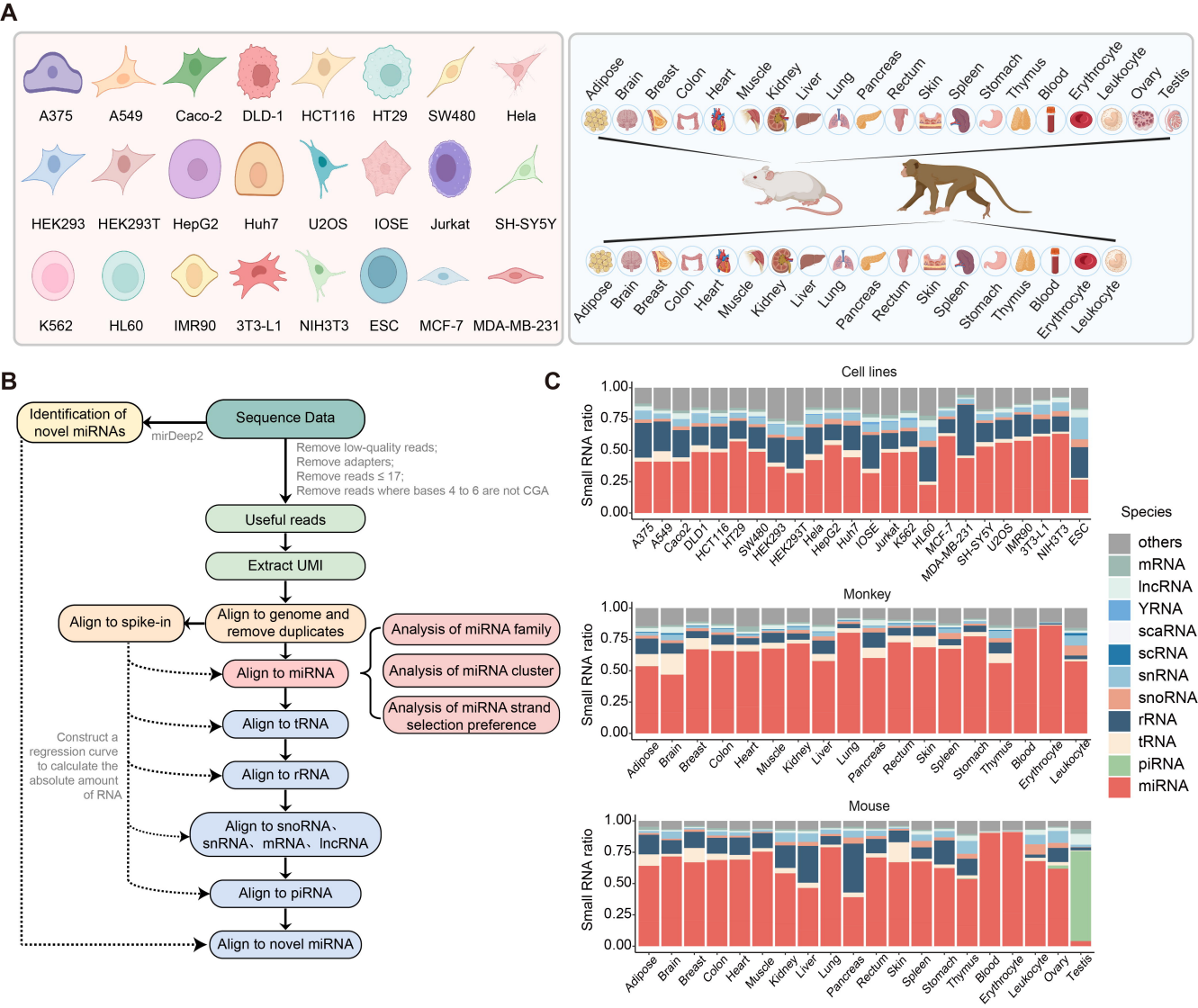
A
A375
A549
Caco-2
DLD-1
HCT116
HT29
SW480
Hela
HEK293
HEK293T
HepG2
Huh7
U2OS
IOSE
Jurkat
SH-SY5Y
K562
HL60
IMR90
3T3-L1
NIH3T3
ESC
MCF-7
MDA-MB-231
Adipose
Brain
Breast
Colon
Heart
Muscle
Kidney
Liver
Lung
Pancreas
Rectum
Skin
Spleen
Stomach
Thymus
Blood
Erythrocyte
Leukocyte
Ovary
Testis
B
Identification of novel miRNAs
mirDeep2
Sequence Data
Remove low-quality reads;
Remove adapters;
Remove reads ≤ 17;
Remove reads where bases 4 to 6 are not CGA
Useful reads
Extract UMI
Align to spike-in
Align to genome and remove duplicates
Analysis of miRNA family
Analysis of miRNA cluster
Analysis of miRNA strand selection preference
Align to miRNA
Align to tRNA
Align to rRNA
Construct a regression curve to calculate the absolute amount of RNA
Align to snoRNA、snRNA、mRNA、lncRNA
Align to piRNA
Align to novel miRNA
C
Cell lines
Small RNA ratio
1.00
0.75
0.50
0.25
0.00
A375
A549
Caco2
DLD1
HCT116
HT29
SW480
HEK293
HEK293T
Hela
HepG2
Huh7
IOSE
Jurkat
K562
HL60
MCF-7
MDA-MB-231
SH-SY5Y
U2OS
IMR90
3T3-L1
NIH3T3
ESC
Monkey
Adipose
Brain
Breast
Colon
Heart
Muscle
Kidney
Liver
Lung
Pancreas
Rectum
Skin
Spleen
Stomach
Thymus
Blood
Erythrocyte
Leukocyte
Mouse
Ovary
Testis
Species
others
mRNA
lncRNA
YRNA
scaRNA
scRNA
snRNA
snoRNA
rRNA
tRNA
piRNA
miRNA

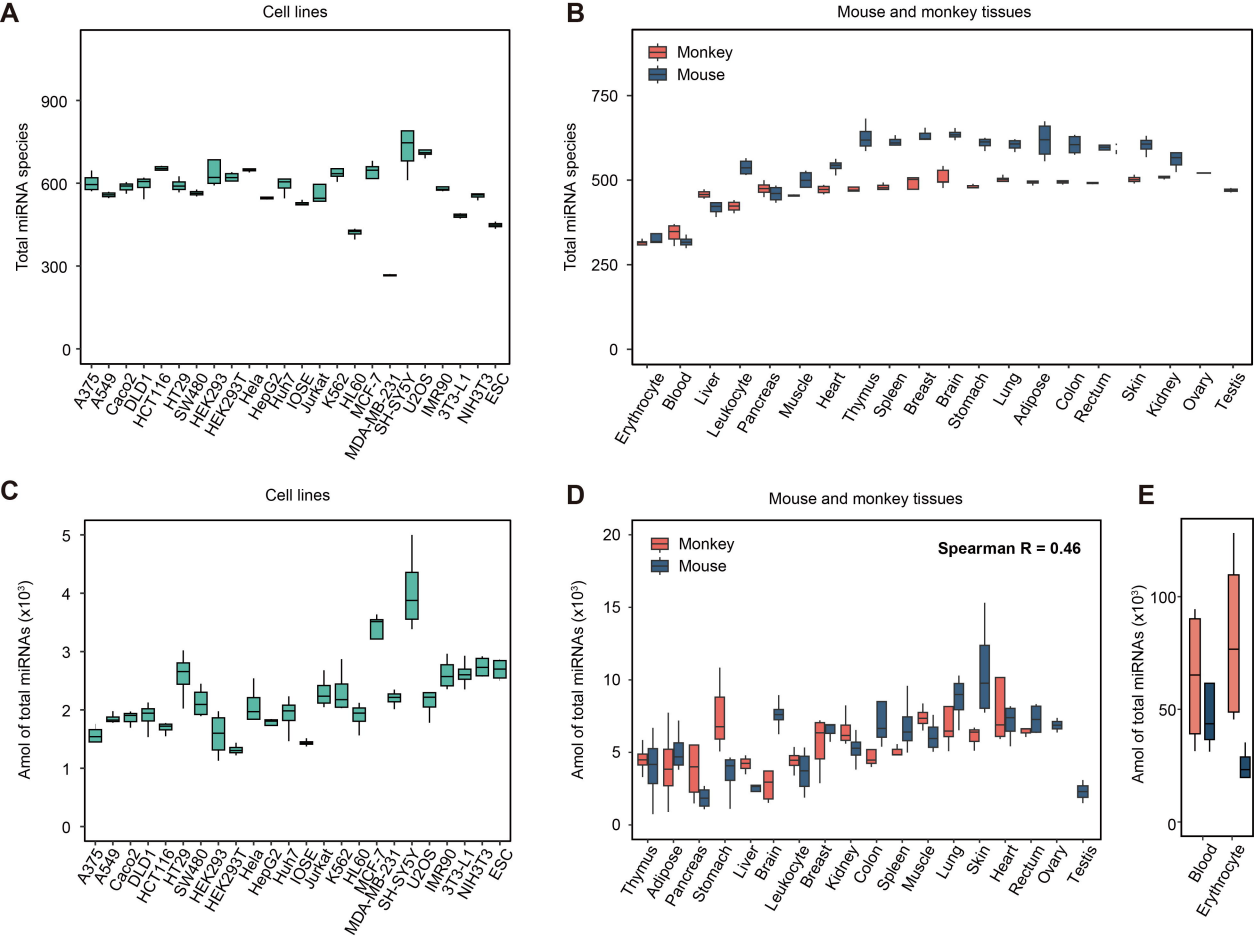
A
Cell lines
Total miRNA species
0
300
600
900
A375
A549
Caco2
DLD1
HCT116
HT29
SW480
HEK293
HEK293T
Hela
HepG2
Huh7
IOSE
Jurkat
K562
HL60
MCF-7
MDA-MB-231
SH-SY5Y
U2OS
IMR90
3T3-L1
NIH3T3
ESC
B
Mouse and monkey tissues
Monkey
Mouse
Total miRNA species
0
250
500
750
Erythrocyte
Blood
Liver
Leukocyte
Pancreas
Muscle
Heart
Thymus
Spleen
Breast
Brain
Stomach
Lung
Adipose
Colon
Rectum
Skin
Kidney
Ovary
Testis
C
Cell lines
Amol of total miRNAs (x10³)
0
1
2
3
4
5
A375
A549
Caco2
DLD1
HCT116
HT29
SW480
HEK293
HEK293T
Hela
HepG2
Huh7
IOSE
Jurkat
K562
HL60
MCF-7
MDA-MB-231
SH-SY5Y
U2OS
IMR90
3T3-L1
NIH3T3
ESC
D
Mouse and monkey tissues
Monkey
Mouse
Spearman R = 0.46
Amol of total miRNAs (x10³)
0
5
10
15
20
Thymus
Adipose
Pancreas
Stomach
Liver
Brain
Leukocyte
Breast
Kidney
Colon
Spleen
Muscle
Lung
Skin
Heart
Rectum
Ovary
Testis
E
Amol of total miRNAs (x10³)
0
50
100
Blood
Erythrocyte

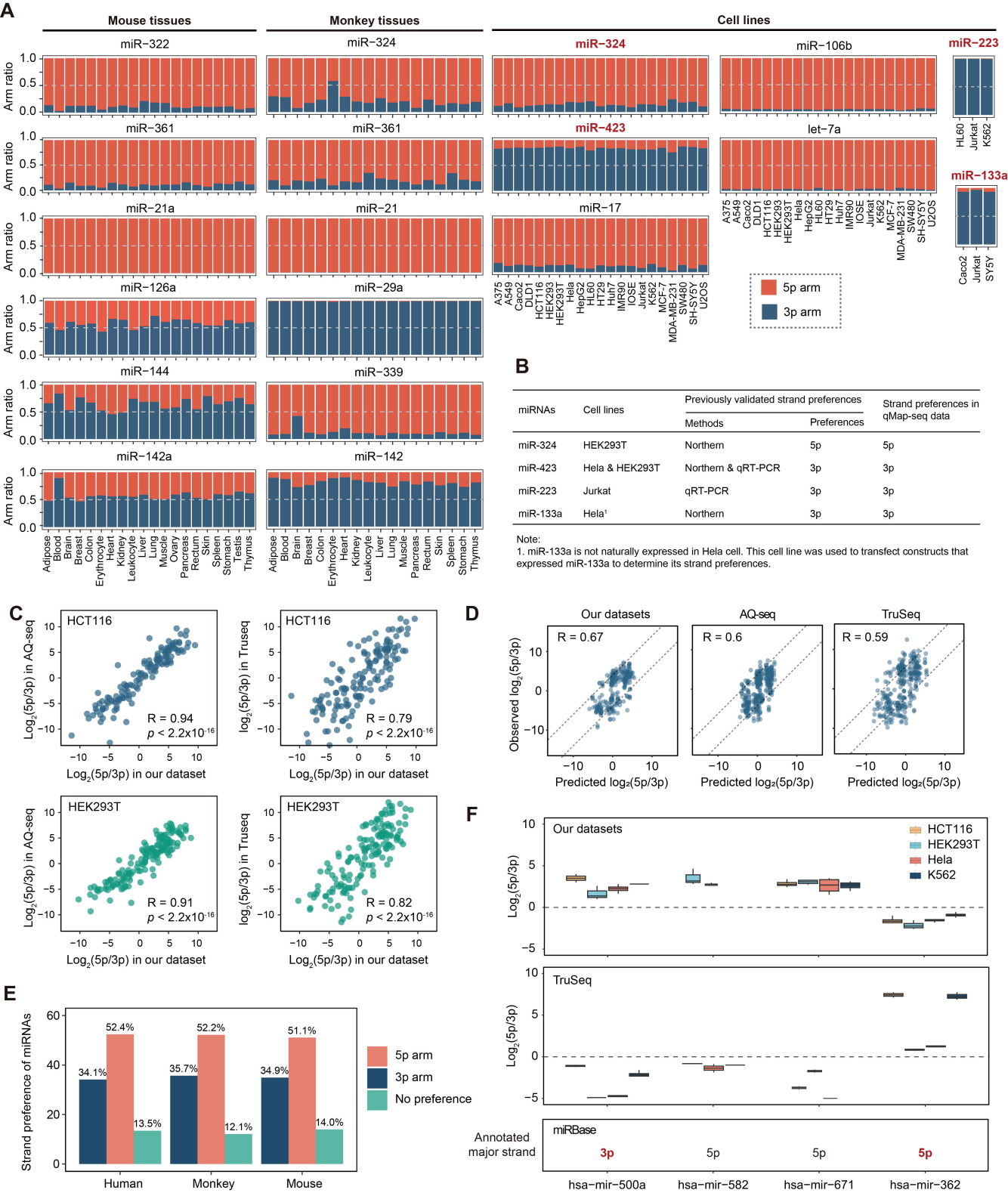

miRNAs	Cell lines	Previously validated strand preferences		Strand preferences in qMap-seq data
		Methods	Preferences	
miR-324	HEK293T	Northern	5p	5p
miR-423	Hela & HEK293T	Northern & qRT-PCR	3p	3p
miR-223	Jurkat	qRT-PCR	3p	3p
miR-133a	Hela[1]	Northern	3p	3p

Note:
1. miR-133a is not naturally expressed in Hela cell. This cell line was used to transfect constructs that expressed miR-133a to determine its strand preferences.

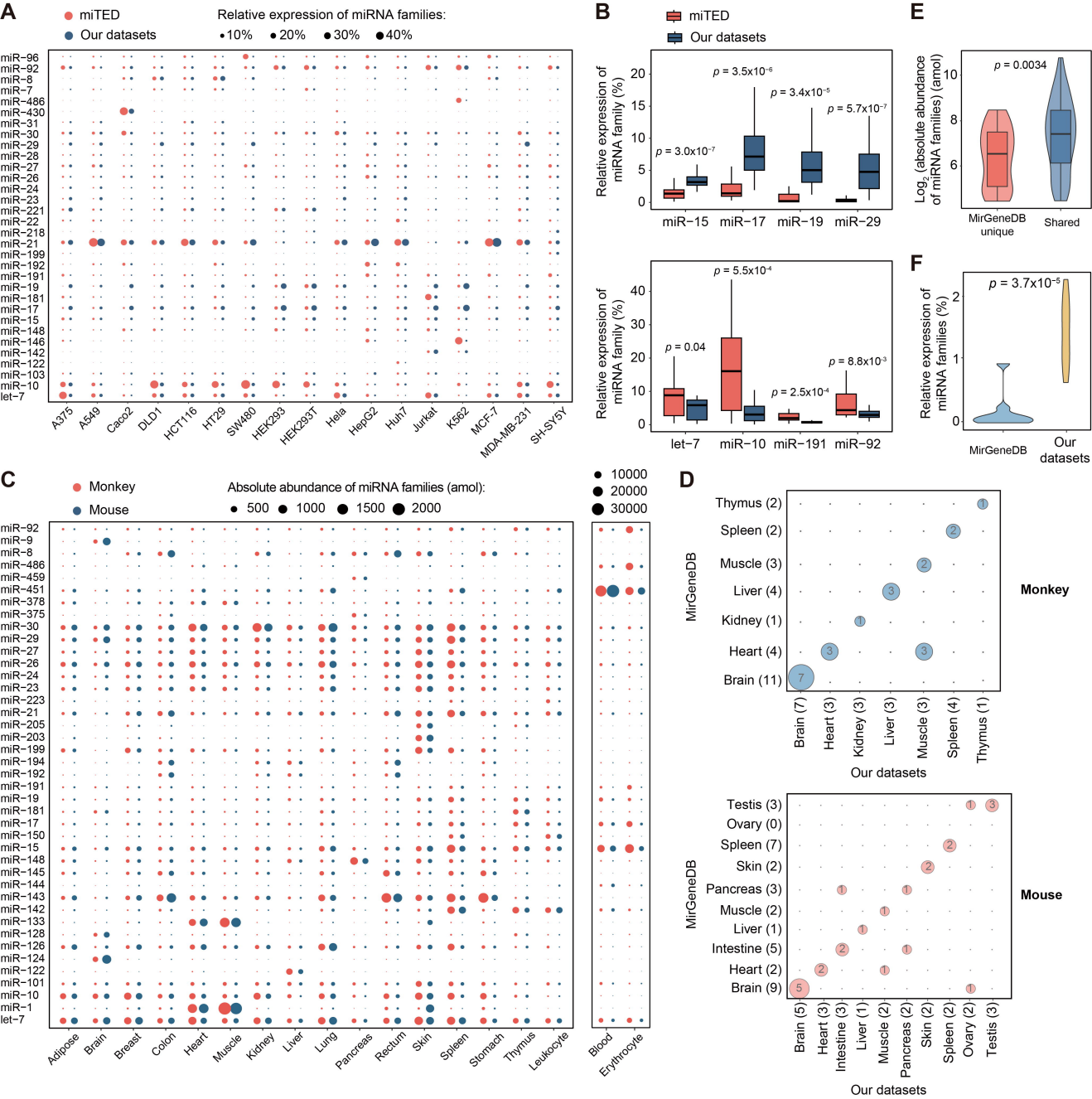
A
miTED
Our datasets
Relative expression of miRNA families:
10%
20%
30%
40%
miR−96
miR−92
miR−8
miR−7
miR−486
miR−430
miR−31
miR−30
miR−29
miR−28
miR−27
miR−26
miR−24
miR−23
miR−221
miR−22
miR−218
miR−21
miR−199
miR−192
miR−191
miR−19
miR−181
miR−17
miR−15
miR−148
miR−146
miR−142
miR−122
miR−103
miR−10
let−7
A375
A549
Caco2
DLD1
HCT116
HT29
SW480
HEK293
HEK293T
Hela
HepG2
Huh7
Jurkat
K562
MCF-7
MDA-MB-231
SH-SY5Y
B
miTED
Our datasets
Relative expression of miRNA family (%)
p = 3.0x10−7
p = 3.5x10−6
p = 3.4x10−5
p = 5.7x10−7
miR−15
miR−17
miR−19
miR−29
p = 0.04
p = 5.5x10−4
p = 2.5x10−4
p = 8.8x10−3
let−7
miR−10
miR−191
miR−92
E
Log2 (absolute abundance of miRNA families) (amol)
p = 0.0034
MirGeneDB unique
Shared
F
Relative expression of miRNA families (%)
p = 3.7x10−5
MirGeneDB
Our datasets
C
Monkey
Mouse
Absolute abundance of miRNA families (amol):
500
1000
1500
2000
10000
20000
30000
miR−92
miR−9
miR−8
miR−486
miR−459
miR−451
miR−378
miR−375
miR−30
miR−29
miR−27
miR−26
miR−24
miR−23
miR−223
miR−21
miR−205
miR−203
miR−199
miR−194
miR−192
miR−191
miR−19
miR−181
miR−17
miR−150
miR−15
miR−148
miR−145
miR−144
miR−143
miR−142
miR−133
miR−128
miR−126
miR−124
miR−122
miR−101
miR−10
miR−1
let−7
Adipose
Brain
Breast
Colon
Heart
Muscle
Kidney
Liver
Lung
Pancreas
Rectum
Skin
Spleen
Stomach
Thymus
Leukocyte
Blood
Erythrocyte
D
MirGeneDB
Thymus (2)
Spleen (2)
Muscle (3)
Liver (4)
Kidney (1)
Heart (4)
Brain (11)
Brain (7)
Heart (3)
Kidney (3)
Liver (3)
Muscle (3)
Spleen (4)
Thymus (1)
Our datasets
Monkey
Testis (3)
Ovary (0)
Spleen (7)
Skin (2)
Pancreas (3)
Muscle (2)
Liver (1)
Intestine (5)
Heart (2)
Brain (9)
Brain (5)
Heart (3)
Intestine (3)
Liver (1)
Muscle (2)
Pancreas (2)
Skin (2)
Spleen (2)
Ovary (2)
Testis (3)
Our datasets
Mouse

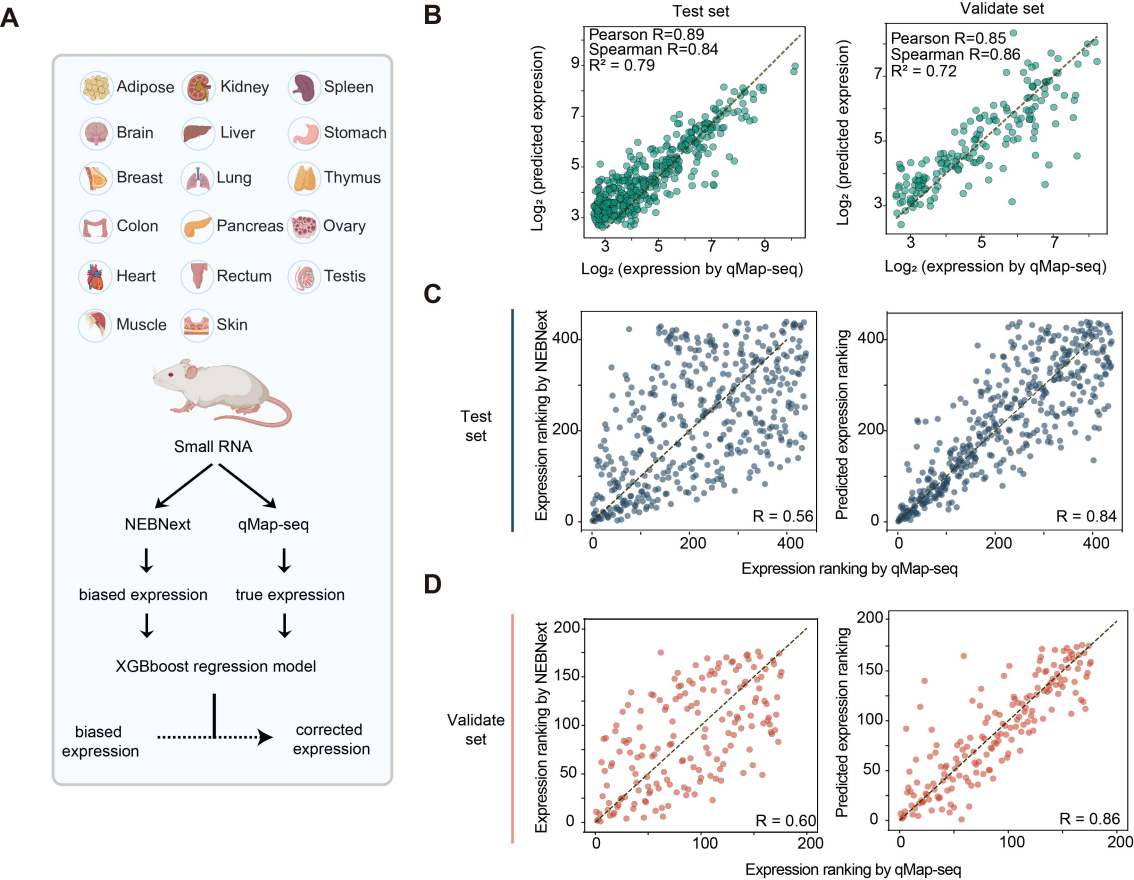
A
Adipose
Kidney
Spleen
Brain
Liver
Stomach
Breast
Lung
Thymus
Colon
Pancreas
Ovary
Heart
Rectum
Testis
Muscle
Skin
Small RNA
NEBNext
qMap-seq
biased expression
true expression
XGBboost regression model
biased expression
corrected expression
B
Test set
Pearson R=0.89
Spearman R=0.84
R² = 0.79
Log₂ (predicted expresion)
Log₂ (expression by qMap-seq)
Validate set
Pearson R=0.85
Spearman R=0.86
R² = 0.72
Log₂ (predicted expresion)
Log₂ (expression by qMap-seq)
C
Test set
Expression ranking by NEBNext
R = 0.56
Predicted expression ranking
R = 0.84
Expression ranking by qMap-seq
D
Validate set
Expression ranking by NEBNext
R = 0.60
Predicted expression ranking
R = 0.86
Expression ranking by qMap-seq

Home

Database

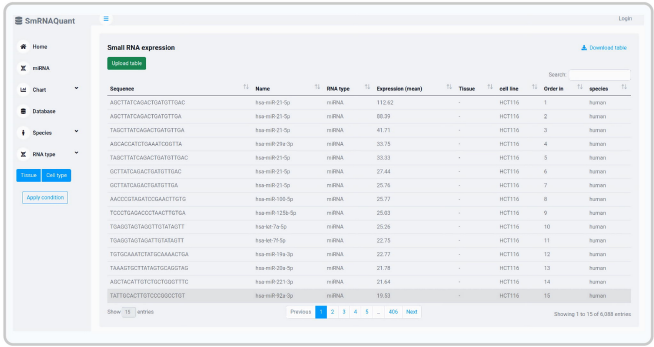

miRNA search

sncRNA profile

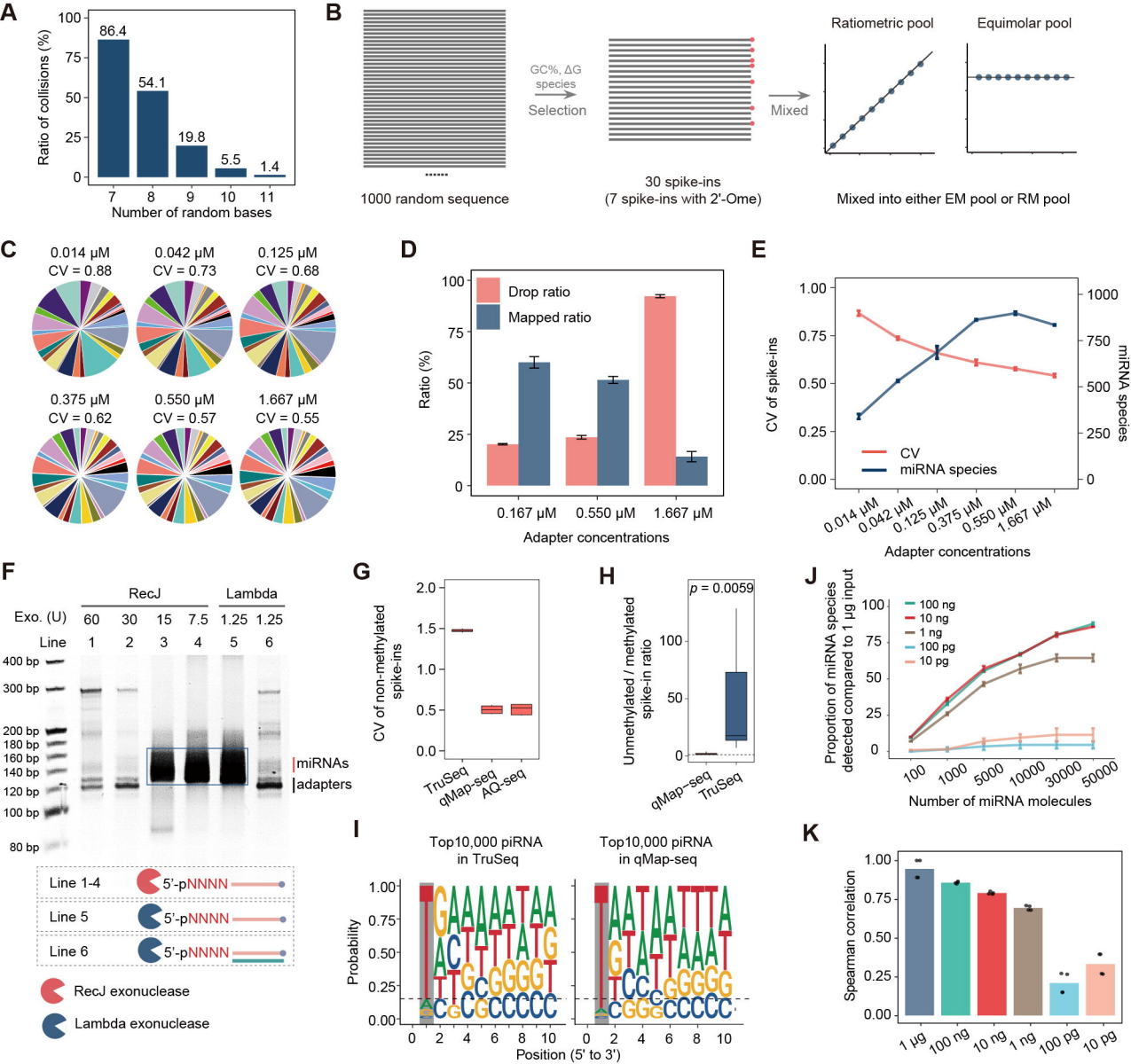
A
Ratio of collisions (%)
86.4
54.1
19.8
5.5
1.4
Number of random bases
B
1000 random sequence
GC%, ΔG species
Selection
30 spike-ins
(7 spike-ins with 2'-Ome)
Mixed
Ratiometric pool
Equimolar pool
Mixed into either EM pool or RM pool
C
0.014 μM CV = 0.88
0.042 μM CV = 0.73
0.125 μM CV = 0.68
0.375 μM CV = 0.62
0.550 μM CV = 0.57
1.667 μM CV = 0.55
D
Drop ratio
Mapped ratio
Ratio (%)
0.167 μM
0.550 μM
1.667 μM
Adapter concentrations
E
CV of spike-ins
miRNA species
CV
miRNA species
Adapter concentrations
F
RecJ
Lambda
Exo. (U)
Line
miRNAs
adapters
Line 1-4
Line 5
Line 6
5'-pNNNN
RecJ exonuclease
Lambda exonuclease
G
CV of non-methylated spike-ins
TruSeq
qMap-seq
AQ-seq
H
p = 0.0059
Unmethylated / methylated spike-in ratio
qMap-seq
TruSeq
J
Proportion of miRNA species detected compared to 1 μg input
100 ng
10 ng
1 ng
100 pg
10 pg
Number of miRNA molecules
I
Top10,000 piRNA in TruSeq
Top10,000 piRNA in qMap-seq
Probability
Position (5' to 3')
K
Spearman correlation
1 μg
100 ng
10 ng
1 ng
100 pg
10 pg

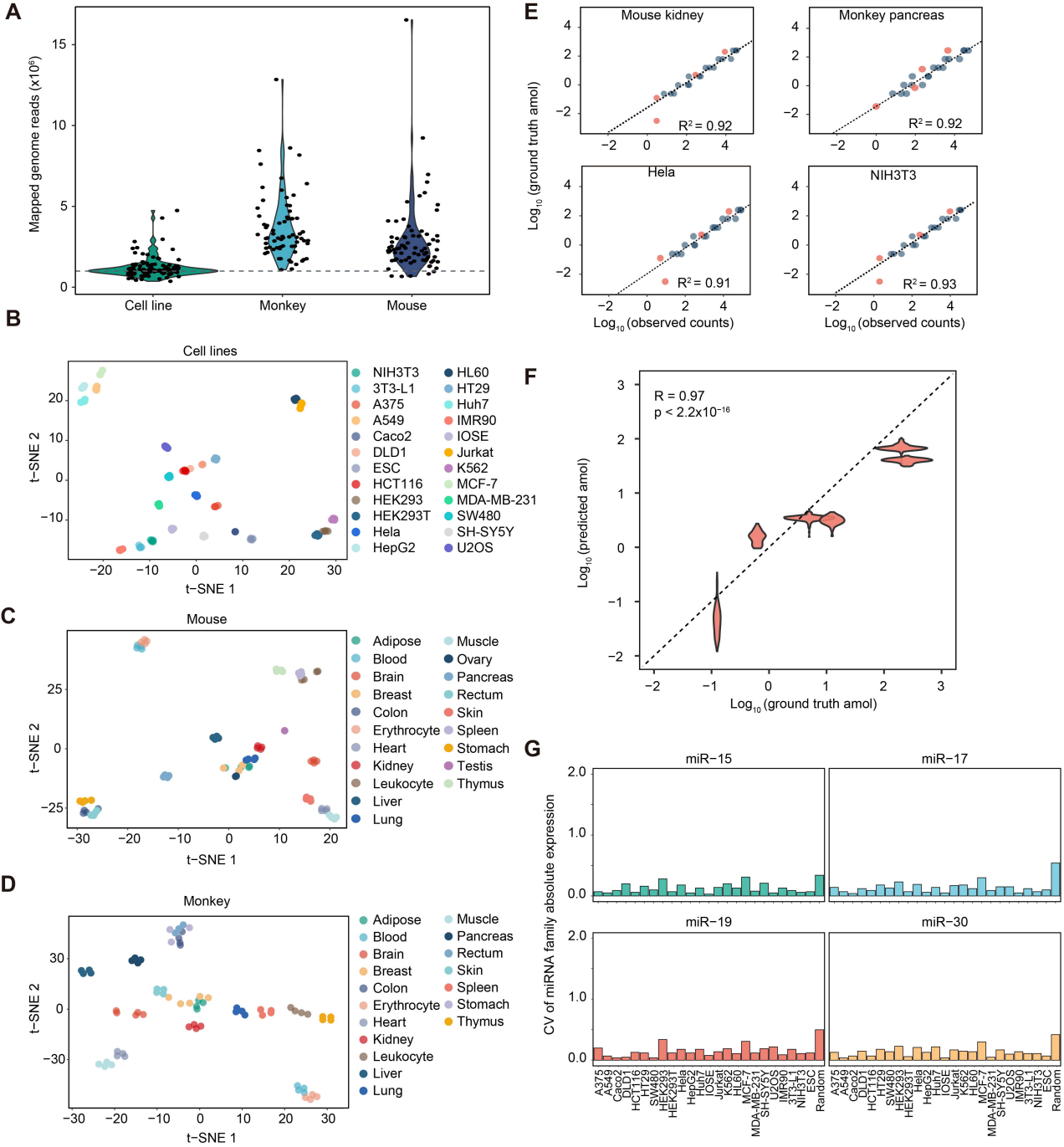
A
Mapped genome reads (x10^6)
Cell line
Monkey
Mouse
B
Cell lines
t−SNE 1
t−SNE 2
NIH3T3
3T3-L1
A375
A549
Caco2
DLD1
ESC
HCT116
HEK293
HEK293T
Hela
HepG2
HL60
HT29
Huh7
IMR90
IOSE
Jurkat
K562
MCF-7
MDA-MB-231
SW480
SH-SY5Y
U2OS
C
Mouse
Adipose
Blood
Brain
Breast
Colon
Erythrocyte
Heart
Kidney
Leukocyte
Liver
Lung
Muscle
Ovary
Pancreas
Rectum
Skin
Spleen
Stomach
Testis
Thymus
D
Monkey
E
Mouse kidney
Monkey pancreas
Hela
NIH3T3
R² = 0.92
R² = 0.92
R² = 0.91
R² = 0.93
Log10 (ground truth amol)
Log10 (observed counts)
F
R = 0.97
p < 2.2x10⁻¹⁶
Log10 (predicted amol)
Log10 (ground truth amol)
G
miR−15
miR−17
miR−19
miR−30
CV of miRNA family absolute expression
Random

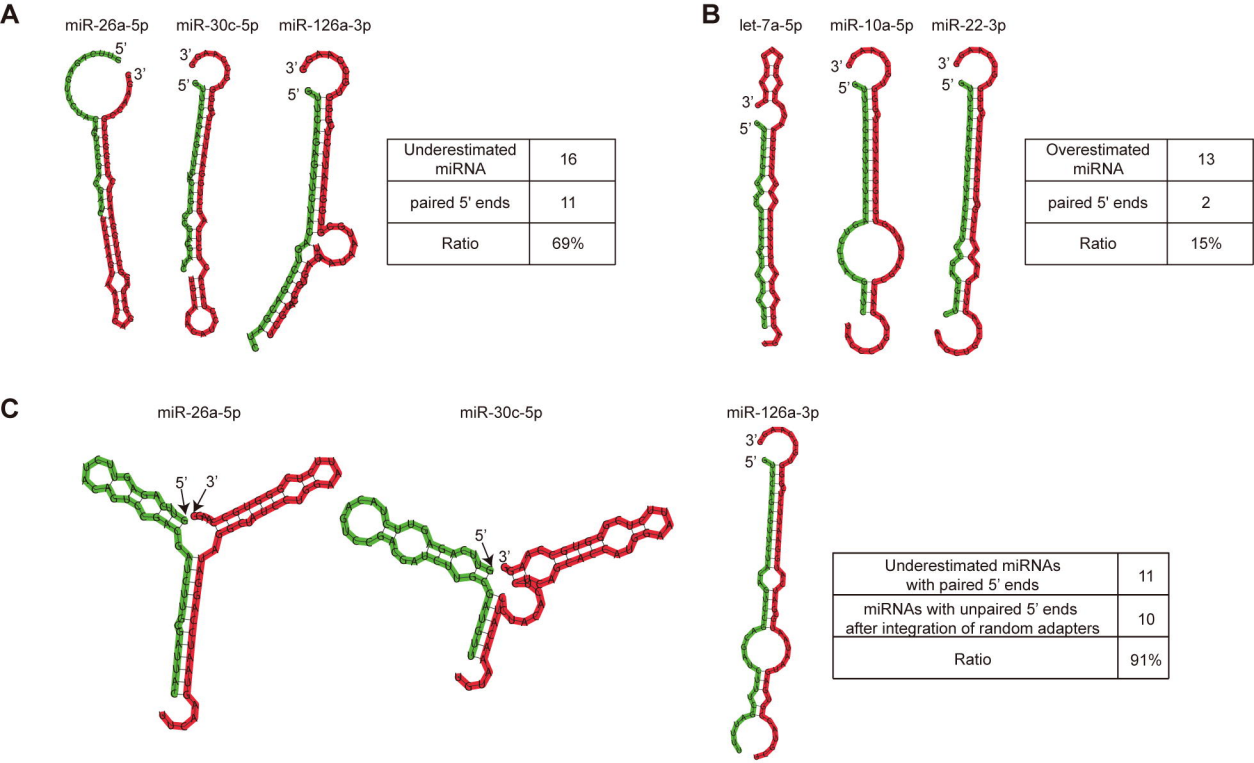

Underestimated miRNA	16
paired 5' ends	11
Ratio	69%

Overestimated miRNA	13
paired 5' ends	2
Ratio	15%

Underestimated miRNAs with paired 5' ends	11
miRNAs with unpaired 5' ends after integration of random adapters	10
Ratio	91%

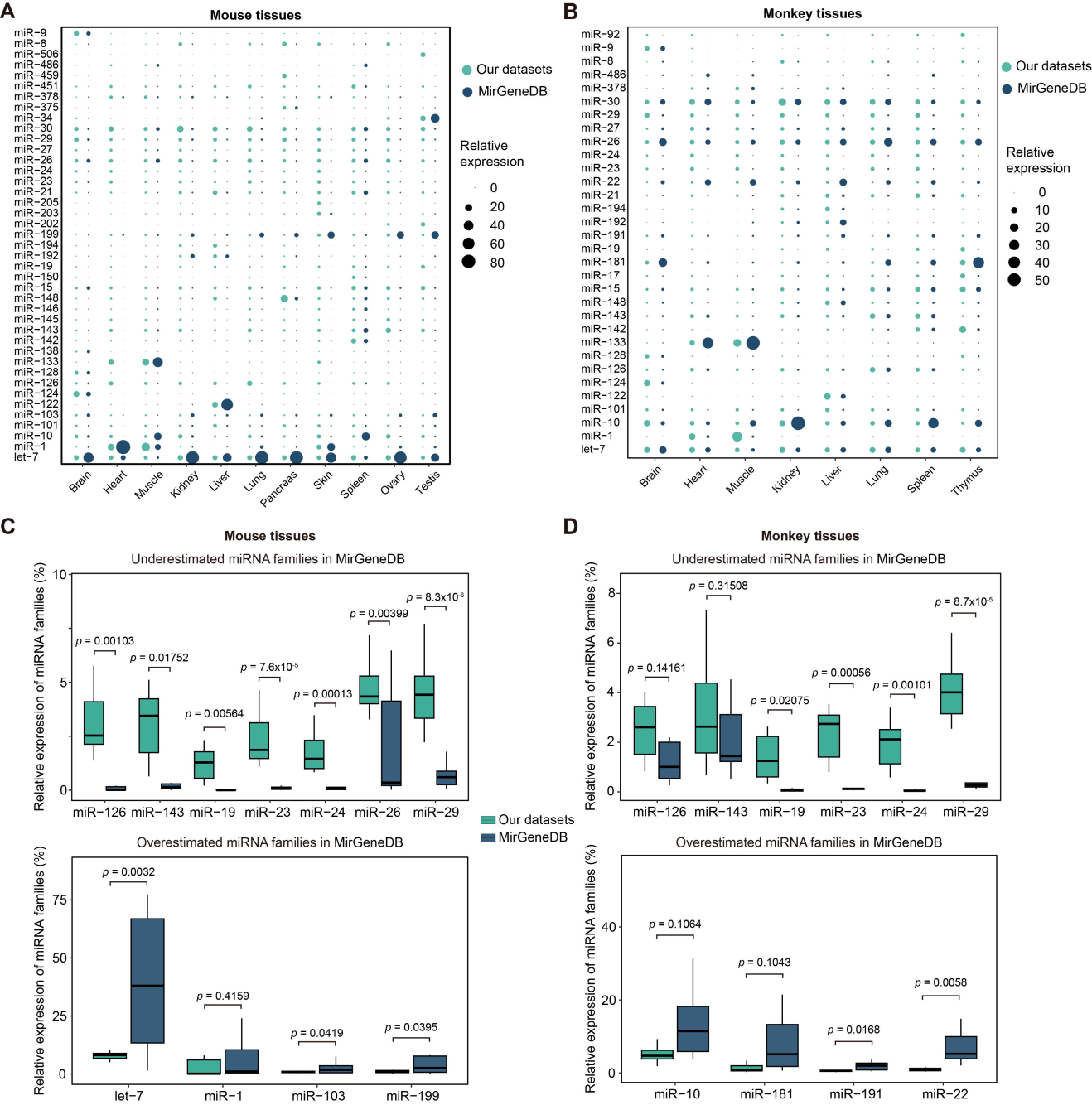
A
Mouse tissues
miR−9
miR−8
miR−506
miR−486
miR−459
miR−451
miR−378
miR−375
miR−34
miR−30
miR−29
miR−27
miR−26
miR−24
miR−23
miR−21
miR−205
miR−203
miR−202
miR−199
miR−194
miR−192
miR−19
miR−150
miR−15
miR−148
miR−146
miR−145
miR−143
miR−142
miR−138
miR−133
miR−128
miR−126
miR−124
miR−122
miR−103
miR−101
miR−10
miR−1
let−7
Brain
Heart
Muscle
Kidney
Liver
Lung
Pancreas
Skin
Spleen
Ovary
Testis
Our datasets
MirGeneDB
Relative expression
0
20
40
60
80
B
Monkey tissues
miR−92
miR−9
miR−8
miR−486
miR−378
miR−30
miR−29
miR−27
miR−26
miR−24
miR−23
miR−22
miR−21
miR−194
miR−192
miR−191
miR−19
miR−181
miR−17
miR−15
miR−148
miR−143
miR−142
miR−133
miR−128
miR−126
miR−124
miR−122
miR−101
miR−10
miR−1
let−7
Brain
Heart
Muscle
Kidney
Liver
Lung
Spleen
Thymus
Our datasets
MirGeneDB
Relative expression
0
10
20
30
40
50
C
Mouse tissues
Underestimated miRNA families in MirGeneDB
Relative expression of miRNA families (%)
p = 0.00103
p = 0.01752
p = 0.00564
p = 7.6x10-5
p = 0.00013
p = 0.00399
p = 8.3x10-6
miR−126
miR−143
miR−19
miR−23
miR−24
miR−26
miR−29
Overestimated miRNA families in MirGeneDB
p = 0.0032
p = 0.4159
p = 0.0419
p = 0.0395
let−7
miR−1
miR−103
miR−199
Our datasets
MirGeneDB
D
Monkey tissues
Underestimated miRNA families in MirGeneDB
Relative expression of miRNA families (%)
p = 0.14161
p = 0.31508
p = 0.02075
p = 0.00056
p = 0.00101
p = 8.7x10-5
miR−126
miR−143
miR−19
miR−23
miR−24
miR−29
Overestimated miRNA families in MirGeneDB
p = 0.1064
p = 0.1043
p = 0.0168
p = 0.0058
miR−10
miR−181
miR−191
miR−22

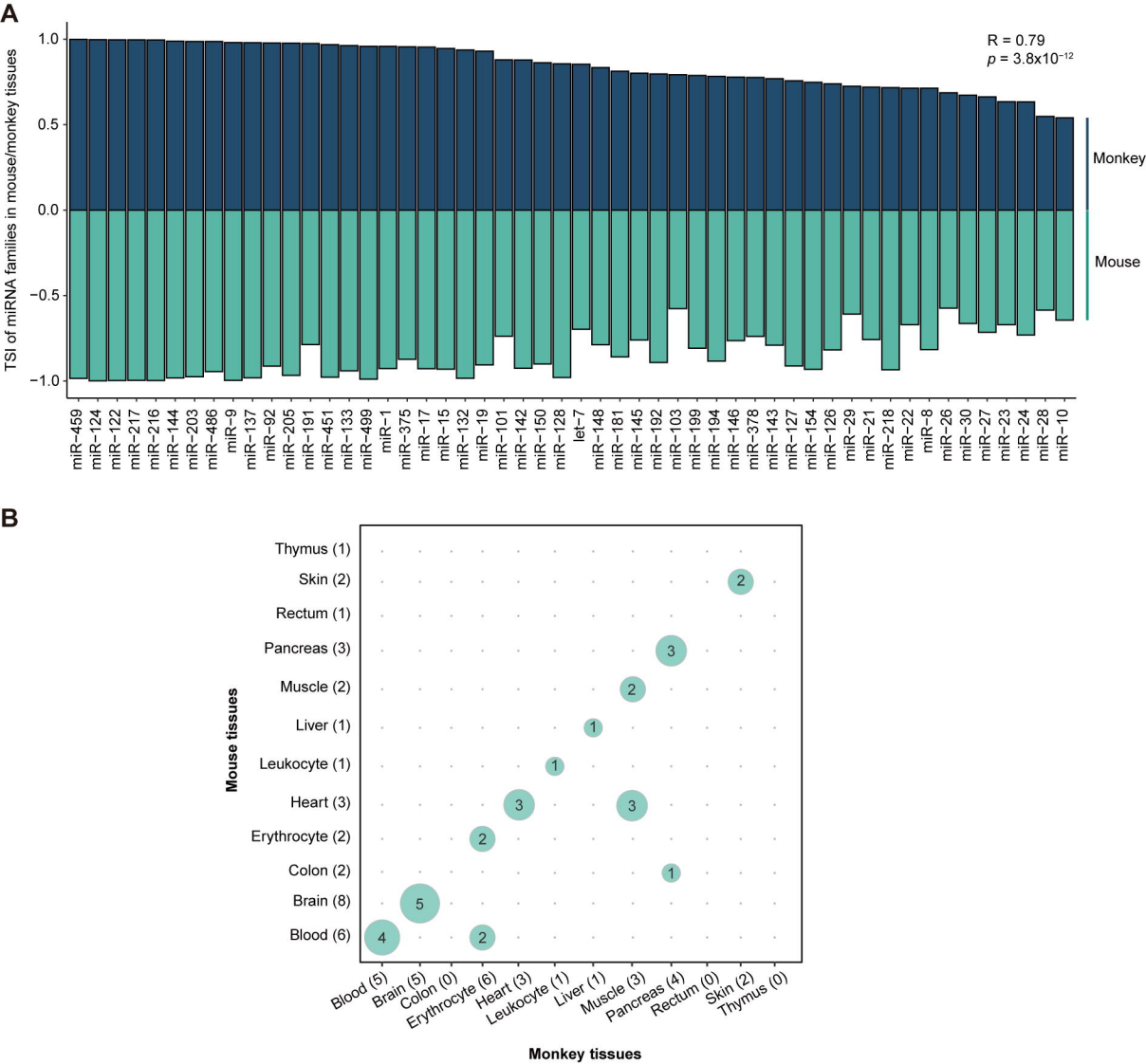
A
R = 0.79
p = 3.8x10−12
TSI of miRNA families in mouse/monkey tissues
1.0
0.5
0.0
−0.5
−1.0
Monkey
Mouse
miR−459
miR−124
miR−122
miR−217
miR−216
miR−144
miR−203
miR−486
miR−9
miR−137
miR−92
miR−205
miR−191
miR−451
miR−133
miR−499
miR−1
miR−375
miR−17
miR−15
miR−132
miR−19
miR−101
miR−142
miR−150
miR−128
let−7
miR−148
miR−181
miR−145
miR−192
miR−103
miR−199
miR−194
miR−146
miR−378
miR−143
miR−127
miR−154
miR−126
miR−29
miR−21
miR−218
miR−22
miR−8
miR−26
miR−30
miR−27
miR−23
miR−24
miR−28
miR−10
B
Mouse tissues
Thymus (1)
Skin (2)
Rectum (1)
Pancreas (3)
Muscle (2)
Liver (1)
Leukocyte (1)
Heart (3)
Erythrocyte (2)
Colon (2)
Brain (8)
Blood (6)
Monkey tissues
Blood (5)
Brain (5)
Colon (0)
Erythrocyte (6)
Heart (3)
Leukocyte (1)
Liver (1)
Muscle (3)
Pancreas (4)
Rectum (0)
Skin (2)
Thymus (0)